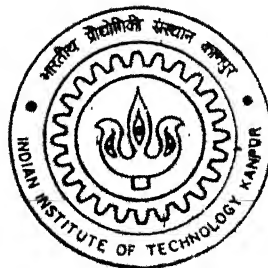


Damage Evaluation in Bulk Metal Forming Processes using DEFORM

By

Bhanu Kishore Battu



DEPARTMENT OF MECHANICAL ENGINEERING

Indian Institute of Technology Kanpur

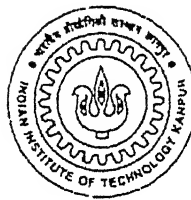
FEBRUARY, 2002

Damage Evaluation in Bulk Metal Forming Processes using DEFORM

A Thesis Submitted
In Partial Fulfillment of the Requirements
for the Degree of
Master of Technology

by

Bhanu Kishore Battu



to the
DEPARTMENT OF MECHANICAL ENGINEERING
INDIAN INSTITUTE OF TECHNOLOGY KANPUR
FEBRUARY, 2002

4 FEB 2003

पुरुषोत्तम कान्तिनाथ जैन मठ पुस्तकालय

भारतीय प्रतिलिपि विभाग बानपुर

अवधि क्र. A-141871



A141871

CERTIFICATE

28-2-02

2.

It is certified that the work contained in the thesis entitled "*Damage Evaluation in Bulk Metal Forming Processes using DEFORM*"; by *Bhanu Kishore Battu*, has been carried out under my supervision and that this work has not been submitted elsewhere for a degree.



Dr. N. V. Reddy

Asst. Professor

Dept. of Mechanical Engineering

I.I.T Kanpur

FEBRUARY, 2002

Acknowledgements

At the outset, I would like to express my heartfelt gratitude to my thesis supervisor Dr. N. Venkata Reddy for his invaluable help, constant encouragement and sagacious advice throughout my M.tech. program. His effective guidance, dynamism, coupled with his clarity of thoughts has directed the work toward completion. I feel very happy and fortunate to have the opportunity to work with him and I shall always remain obliged to him for devoting a large share of his valuable time and knowledge to this work. It is not possible to express my full gratitude to him in the above few words.

I am especially thankful to Dr. G. K. Lal and Dr. Raghuram for providing lab facility.

I am thankful to my colleagues for their constant help and encouragement. But for the constant encouragement of my friends I would not have completed this work. Yugandar, Rahul, Behara, Saurabh, Roy all deserve acknowledgement. Special thanks are to P.L.N., Ganesh, Ajit, and Bandaru.

I shall be always grateful to those invisible persons whose support cannot be expressed in words.

Bhanu Kishore

*To
my mother
and
father Late Rama Mohana Rao*

Abstract

The occurrence of ductile fracture is the major limiting factor that determines the workability of cold bulk metal forming processes. Prediction of ductile fracture initiation will allow prior modification of the process which results in defect free product.

The common defects that occur in upsetting and backward extrusion are surface cracks. The consequence of this defect is not only limited to less productivity but also causes damage to punch. Fracture occurrence can be prevented by choosing the proper process variables using mathematical modeling.

In the present work, DEFORM software is used to predict the damage in bulk metal forming processes. User defined programs are added to the software to determine the damage. Critical damage criterion [Dhar et al.], Oyane's criterion and Cockcroft and Latham criteria are used to predict the damage in upsetting and backward extrusion processes. For typical values of input variables, the damage, hydrostatic stress and circumferential stress are studied. A detailed parametric study is carried out to show the effects of the coefficient of friction, geometric ratios for different types of workpieces. The material is assumed to be elasto-plastic and strain hardening. Coulomb's friction law is used to model the friction at the die-work interface. Critical damage criterion is used to analyze the damage prediction for cylindrical and cubical workpieces. Oyane's criterion is used to study the damage for cylindrical workpiece. For backward extrusion, Cockcroft and Latham criterion is used.

The studies of Critical damage criterion to the cylindrical and cubical workpieces show that the micro-crack first initiates along the free edges of the die-work interface, then at the center of the workpiece and proceeded to the meridian surface. The fracture will appear first at the meridian surface since the hydrostatic stress is minimum compressive and the circumferential stress is maximum tensile. From the parametric study, as the friction increases, fracture occurs at lower reduction. Micro-crack initiates at lower reduction for height to diameter ratio equals to one, as compared with other values. Further, with higher height to diameter ratio, there is a possibility to form a cavity at the center of the workpiece due to minimum compressive hydrostatic stresses.

The study of Oyane's criterion to the cylindrical workpiece shows that, the pattern of damage and hydrostatic stress distribution is same as that of Critical damage criterion, but these two criteria are considered for two different materials.

In backward extrusion, Cockcroft and Latham criterion shows that the micro-crack initiates at corner of the punch-work interface. The hydrostatic stress at that location is

first compressive and as the process goes on it becomes tensile, which lead to fracture. From the parametric study, it is observed that with decrease in punch nose face angle, the damage value increases.

Contents

List of Figures	iii
List of Symbols	viii
1 INTRODUCTION	1
1.1 Literature Review	2
1.1.1 Deformation Analysis of Forging Process	2
1.1.2 Deformation Analysis of Backward Extrusion	5
1.1.3 Ductile Fracture Criteria	6
1.1.4 Defects in Forging	15
1.2 Scope and Objective of the Present Work	17
1.3 Organization of Thesis	18
2 FORMULATION	19
2.1 Introduction	19
2.2 DEFORM - An Introduction	20
2.2.1 Object Modeling	20
2.2.2 Adding user defined programs	21
2.3 Boundary Conditions	22
2.3.1 Upsetting of Cylindrical Workpiece	22
2.3.2 Upsetting of Cubical Workpiece	23
2.3.3 Backward Extrusion of a cylindrical workpiece with cylindrical punch	24
2.4 Implementation Procedure of Ductile Fracture Criteria	25
2.4.1 Critical Damage Criterion [Dhar et al.]	25
2.4.2 Oyane's Criterion	26
2.4.3 Cockcroft and Latham criterion	27

3	RESULTS AND DISCUSSION	28
3.1	Predictions using Critical Damage Criterion [Dhar et al.]	29
3.1.1	Axisymmetric upsetting - cylindrical workpiece	29
3.1.2	Three dimensional upsetting - cubical workpiece	32
3.2	Predictions using Oyane's Criterion	34
3.2.1	Upsetting of cylindrical workpiece	34
3.3	Analysis of Backward Extrusion	37
4	CONCLUSIONS AND SCOPE FOR FUTURE WORK	65

List of Figures

2.1	Domain for cylindrical workpiece forging	22
2.2	Domain used for cubical workpiece upsetting	24
2.3	Domain used for backward extrusion	25
3.1	Domain used for axisymmetric upsetting	29
3.2	Domain used for three dimensional upsetting	32
3.3	Domain used for backward extrusion	38
3.4	Backward extrusion : punch dimensions	38
3.5	Damage distribution of cylindrical block at 24% reduction [Material AISI 1090 steel, $\bar{\sigma} = 1115\bar{\epsilon}^{0.19} + 464$ Mpa, h= 25mm, d= 25 mm, $\mu=0.1$]	39
3.6	Damage distribution of cylindrical block at 28% reduction [Material AISI 1090 steel, $\bar{\sigma} = 1115\bar{\epsilon}^{0.19} + 464$ Mpa, h= 25mm, d= 25 mm, $\mu=0.1$]	39
3.7	Damage distribution of cylindrical block at 35.2% reduction [Material AISI 1090 steel, $\bar{\sigma} = 1115\bar{\epsilon}^{0.19} + 464$ Mpa, h= 25mm, d= 25 mm, $\mu=0.1$]	40
3.8	Equivalent strain distribution of cylindrical block at 35.2% reduction [Material AISI 1090 steel, $\bar{\sigma} = 1115\bar{\epsilon}^{0.19} + 464$ Mpa, h= 25mm, d= 25 mm, $\mu=0.1$]	40
3.9	Hydrostatic stress distribution of cylindrical block at 24% reduction [Material AISI 1090 steel, $\bar{\sigma} = 1115\bar{\epsilon}^{0.19} + 464$ Mpa, h= 25mm, d= 25 mm, $\mu=0.1$]	41
3.10	Hydrostatic stress distribution of cylindrical block at 28% reduction [Material AISI 1090 steel, $\bar{\sigma} = 1115\bar{\epsilon}^{0.19} + 464$ Mpa, h= 25mm, d= 25 mm, $\mu=0.1$]	41
3.11	Hydrostatic stress distribution of cylindrical block at 35.2% reduction [Material AISI 1090 steel, $\bar{\sigma} = 1115\bar{\epsilon}^{0.19} + 464$ Mpa, h= 25mm, d= 25 mm, $\mu=0.1$]	42

3.12	Circumferential stress distribution of cylindrical block at 24% reduction [Material AISI 1090 steel, $\bar{\sigma} = 1115\bar{\epsilon}^{0.19} + 464$ Mpa, $h= 25\text{mm}$, $d= 25$ mm, $\mu=0.1$]	42
3.13	Circumferential stress distribution of cylindrical block at 28% reduction [Material AISI 1090 steel, $\bar{\sigma} = 1115\bar{\epsilon}^{0.19} + 464$ Mpa, $h= 25\text{mm}$, $d= 25$ mm, $\mu=0.1$]	43
3.14	Circumferential stress distribution of cylindrical block at 35.2% reduction [Material AISI 1090 steel, $\bar{\sigma} = 1115\bar{\epsilon}^{0.19} + 464$ Mpa, $h= 25\text{mm}$, $d= 25$ mm, $\mu=0.1$]	43
3.15	Damage distribution of cylindrical block at 36.8% reduction [Material AISI 1090 steel, $\bar{\sigma} = 1115\bar{\epsilon}^{0.19} + 464$ Mpa, $h= 25\text{mm}$, $d= 25$ mm, $\mu=0.05$]	44
3.16	Hydrostatic stress distribution of cylindrical block at 36.8% reduction [Ma- terial AISI 1090 steel, $\bar{\sigma} = 1115\bar{\epsilon}^{0.19} + 464$ Mpa, $h= 25\text{mm}$, $d= 25$ mm, $\mu=0.05$]	44
3.17	Circumferential stress distribution of cylindrical block at 36.8% reduction [Material AISI 1090 steel, $\bar{\sigma} = 1115\bar{\epsilon}^{0.19} + 464$ Mpa, $h= 25\text{mm}$, $d= 25$ mm, $\mu=0.05$]	45
3.18	Effect of damage with varying friction [Material AISI 1090 steel, $\bar{\sigma} =$ $1115\bar{\epsilon}^{0.19} + 464$ Mpa, $h= 25\text{mm}$, $d= 25$ mm]	45
3.19	Damage distribution of cylindrical block at 40% reduction [Material AISI 1090 steel, $\bar{\sigma} = 1115\bar{\epsilon}^{0.19} + 464$ Mpa, $h/d= 0.5$, $d= 25$ mm, $\mu=0.1$]	46
3.20	Hydrostatic stress distribution of cylindrical block at 40% reduction [Ma- terial AISI 1090 steel, $\bar{\sigma} = 1115\bar{\epsilon}^{0.19} + 464$ Mpa, $h/d=0.5$, $d= 25$ mm, $\mu=0.1$] 46	46
3.21	Circumferential stress distribution of cylindrical block at 40% reduction [Material AISI 1090 steel, $\bar{\sigma} = 1115\bar{\epsilon}^{0.19} + 464$ Mpa, $h/d=0.5$, $d= 25$ mm, $\mu=0.1$]	47
3.22	Effect of damage with varying geometric ratios [Material AISI 1090 steel, $\bar{\sigma} = 1115\bar{\epsilon}^{0.19} + 464$ Mpa, $\mu = 0.1$]	47
3.23	Damage distribution at the interface of cubical block at 39.2% reduction [Material AISI 1090 steel, $\bar{\sigma} = 1115\bar{\epsilon}^{0.19} + 464$ Mpa, $2h= 25\text{mm}$, $2a= 25$ mm, $2b= 25\text{mm}$, $\mu=0.1$]	48
3.24	Damage distribution at the center of cubical block at 39.2% reduction [Ma- terial AISI 1090 steel, $\bar{\sigma} = 1115\bar{\epsilon}^{0.19} + 464$ Mpa, $2h= 25\text{mm}$, $2a= 25\text{mm}$, $2b= 25$ mm, $\mu=0.1$]	48

3.25	Hydrostatic stress distribution at the interface of cubical block at 39.2% reduction [Material AISI 1090 steel, $\bar{\sigma} = 1115\bar{\epsilon}^{0.19} + 464$ Mpa, $2h = 25$ mm, $2a = 25$ mm, $2b = 25$ mm, $\mu = 0.1$]	49
3.26	Hydrostatic stress distribution at the center of cylindrical block at 39.2% reduction [Material AISI 1090 steel, $\bar{\sigma} = 1115\bar{\epsilon}^{0.19} + 464$ Mpa, $2h = 25$ mm, $2a = 25$ mm, $2b = 25$ mm, $\mu = 0.1$]	49
3.27	Damage distribution at the interface of cubical block at 32.8% reduction [Material AISI 1090 steel, $\bar{\sigma} = 1115\bar{\epsilon}^{0.19} + 464$ Mpa, $2h = 25$ mm, $2a = 25$ mm, $2b = 25$ mm, $\mu = 0.2$]	50
3.28	Damage distribution at the center of cubical block at 32.8% reduction [Material AISI 1090 steel, $\bar{\sigma} = 1115\bar{\epsilon}^{0.19} + 464$ Mpa, $2h = 25$ mm, $2a = 25$ mm, $2b = 25$ mm, $\mu = 0.2$]	50
3.29	Hydrostatic stress distribution at the interface of cubical block at 32.8% reduction [Material AISI 1090 steel, $\bar{\sigma} = 1115\bar{\epsilon}^{0.19} + 464$ Mpa, $2h = 25$ mm, $2a = 25$ mm, $2b = 25$ mm, $\mu = 0.2$]	51
3.30	Hydrostatic stress distribution at the center of cubical block at 32.8% reduction [Material AISI 1090 steel, $\bar{\sigma} = 1115\bar{\epsilon}^{0.19} + 464$ Mpa, $2h = 25$ mm, $2a = 25$ mm, $2b = 25$ mm, $\mu = 0.2$]	52
3.31	Damage distribution at the interface of cubical block at 39.2% reduction [Material AISI 1090 steel, $\bar{\sigma} = 1115\bar{\epsilon}^{0.19} + 464$ Mpa, $h/a = 0.5$, $a/b = 1$, $2a = 25$ mm, $\mu = 0.1$]	52
3.32	Damage distribution at the center of cubical block at 39.2% reduction [Material AISI 1090 steel, $\bar{\sigma} = 1115\bar{\epsilon}^{0.19} + 464$ Mpa, $h/a = 0.5$, $a/b = 1$, $2a = 25$ mm, $\mu = 0.1$]	53
3.33	Hydrostatic stress distribution at the interface of cubical block at 39.2% reduction [Material AISI 1090 steel, $\bar{\sigma} = 1115\bar{\epsilon}^{0.19} + 464$ Mpa, $h/a = 0.5$, $a/b = 1$, $2a = 25$ mm, $\mu = 0.1$]	53
3.34	Hydrostatic stress distribution at the center of cubical block at 39.2% reduction [Material AISI 1090 steel, $\bar{\sigma} = 1115\bar{\epsilon}^{0.19} + 464$ Mpa, $h/a = 0.5$, $a/b = 1$, $2a = 25$ mm, $\mu = 0.1$]	54
3.35	Damage distribution at the interface of cubical block at 40.8% reduction [Material AISI 1090 steel, $\bar{\sigma} = 1115\bar{\epsilon}^{0.19} + 464$ Mpa, $a/b = 0.5$, $h/a = 1$, $2a = 25$ mm, $\mu = 0.1$]	54

3.36	Damage distribution at the center of cubical block at 40.8% reduction [Material AISI 1090 steel, $\bar{\sigma} = 1115\bar{\epsilon}^{0.19} + 464$ Mpa, $a/b = 0.5$, $h/a = 1$, $2a = 25$ mm, $\mu = 0.1$]	55
3.37	Hydrostatic stress distribution at the interface of cubical block at 40.8% reduction [Material AISI 1090 steel, $\bar{\sigma} = 1115\bar{\epsilon}^{0.19} + 464$ Mpa, $a/b = 0.5$, $h/a = 1$, $2a = 25$ mm, $\mu = 0.1$]	56
3.38	Hydrostatic stress distribution at the center of cylindrical block at 40.8% reduction [Material AISI 1090 steel, $\bar{\sigma} = 1115\bar{\epsilon}^{0.19} + 464$ Mpa, $a/b = 0.5$, $h/a = 1$, $2a = 25$ mm, $\mu = 0.1$]	56
3.39	Damage distribution of cylindrical block at 33.6% reduction [Material UNI 3571, $\bar{\sigma} = 574\bar{\epsilon}^{0.141} + 300$ Mpa, $h = 25$ mm, $d = 25$ mm, $\mu = 0.1$]	57
3.40	Hydrostatic stress distribution of cylindrical block at 33.6% reduction [Material UNI 3571, $\bar{\sigma} = 574\bar{\epsilon}^{0.141} + 300$ Mpa, $h = 25$ mm, $d = 25$ mm, $\mu = 0.1$]	57
3.41	Circumferential stress distribution of cylindrical block at 33.6% reduction [Material UNI 3571, $\bar{\sigma} = 574\bar{\epsilon}^{0.141} + 300$ Mpa, $h = 25$ mm, $d = 25$ mm, $\mu = 0.1$]	58
3.42	Damage distribution of cylindrical block at 37.6% reduction [Material UNI 3571, $\bar{\sigma} = 574\bar{\epsilon}^{0.141} + 300$ Mpa, $h = 25$ mm, $d = 25$ mm, $\mu = 0.05$]	58
3.43	Hydrostatic stress distribution of cylindrical block at 37.6% reduction [Material UNI 3571, $\bar{\sigma} = 574\bar{\epsilon}^{0.141} + 300$ Mpa, $h = 25$ mm, $d = 25$ mm, $\mu = 0.05$]	59
3.44	Circumferential stress distribution of cylindrical block at 37.6% reduction [Material UNI 3571, $\bar{\sigma} = 574\bar{\epsilon}^{0.141} + 300$ Mpa, $h = 25$ mm, $d = 25$ mm, $\mu = 0.05$]	59
3.45	Damage distribution of cylindrical block at 35.2% reduction [Material UNI 3571, $\bar{\sigma} = 574\bar{\epsilon}^{0.141} + 300$ Mpa, $h/d = 0.5$, $d = 25$ mm, $\mu = 0.1$]	60
3.46	Hydrostatic stress distribution of cylindrical block at 35.2% reduction [Material UNI 3571, $\bar{\sigma} = 574\bar{\epsilon}^{0.141} + 300$ Mpa, $h/d = 0.5$, $d = 25$ mm, $\mu = 0.1$]	60
3.47	Circumferential stress distribution of cylindrical block at 35.2% reduction [Material UNI 3571, $\bar{\sigma} = 574\bar{\epsilon}^{0.141} + 300$ Mpa, $h/d = 0.5$, $d = 25$ mm, $\mu = 0.1$]	61
3.48	Distribution hydrostatic stress using punch 1 after 6mm movement in backward extrusion [Material UNI 3571, $\bar{\sigma} = 574\bar{\epsilon}^{0.141} + 300$ Mpa, $h = 50$ mm, $d = 104$ mm, $\mu = 0.1$]	61
3.49	Distribution hydrostatic stress using punch 2 after 6mm movement in backward extrusion [Material UNI 3571, $\bar{\sigma} = 574\bar{\epsilon}^{0.141} + 300$ Mpa, $h = 50$ mm, $d = 104$ mm, $\mu = 0.1$]	62

3.50	Variation of hydrostatic stress during backward extrusion process at different points [Material UNI 3571, $\bar{\sigma} = 574\bar{\epsilon}^{0.141} + 300$ Mpa, h= 50mm, d= 104 mm, $\mu=0.05$]	62
3.51	Variation of damage during backward extrusion process at different points [Material UNI 3571, $\bar{\sigma} = 574\bar{\epsilon}^{0.141} + 300$ Mpa, h= 50 mm, d= 104 mm, $\mu=0.1$]	63
3.52	Distribution damage using punch 1, after 6mm movement in backward extrusion [Material UNI 3571, $\bar{\sigma} = 574\bar{\epsilon}^{0.141} + 300$ Mpa, h= 50 mm, d= 104 mm, $\mu=0.1$]	63
3.53	Distribution damage using punch 2, after 6mm movement in backward extrusion [Material UNI 3571, $\bar{\sigma} = 574\bar{\epsilon}^{0.141} + 300$ Mpa, h= 50 mm, d= 104 mm, $\mu=0.1$]	64
3.54	View of workpiece after 6mm movement of punch 2 in backward extrusion [Material UNI 3571, $\bar{\sigma} = 574\bar{\epsilon}^{0.141} + 300$ Mpa, h= 50 mm, d= 104 mm, $\mu=0.1$]	64

List of Symbols

a_1	Constant used in Critical damage criterion.
a_2	Constant used in Critical damage criterion.
A	Constant used in Oyane's criterion.
C_2	Damage variable used in Cockcroft and Latham Criterion.
C_D	Constant used in Critical damage criterion.
D	Damage variable used in Critical damage criterion.
D_{oy}	Damage variable used in Oyane's criterion.
E	Young's modulus.
K	Hardening coefficient.
n	Hardening exponent.
ΔU_x	Incremental displacement in X- direction.
ΔU_y	Incremental displacement in Y- direction.
ΔU_z	Incremental displacement in Z- direction.
μ	Coefficient of friction.
$\bar{\epsilon}$	Effective strain.
$\dot{\epsilon}$	Strain rate.
$\bar{\sigma}$	Effective stress.
σ_1	Maximum normal stress.
σ_m	Hydrostatic stress.

Chapter 1

INTRODUCTION

Forming is a production process that in most of the cases, it gives the final shape of the metal products and at the same time significantly influences resulting properties of the products. The occurrence of ductile fracture is the major limiting factor that determines the workability of cold bulk metal forming processes. Prediction of ductile fracture initiation will allow prior modification of the process which results in defect free product. Forging is a process in which the workpiece is shaped by compressive forces applied through various dies and tools. It was first used to make jewelry, coins and various implements. From a simple rivet to the landing gear of aircraft, from a connecting rod of an automobile to the propeller shaft of ship, forged products have a wide spectrum of applications today. The reason for this is that forged parts possess good strength and toughness. These properties are achieved because the grain orientation and grain size can be controlled in forging process.

Extrusion is also one type of forging process where the compressive forces are used to obtain final shaped products. The basic or primary operations of cold extrusion are forward extrusion, backward extrusion and radial extrusion. It is commonly accepted practice to classify extrusion operation according to the direction relationships between the material flow and the punch movement. The process of backward extrusion (also called inverse extrusion, impact extrusion, or piercing) is utilized to produce hollow shells from solid rods or disks. Schematically, a disk (slug) is placed in the cavity of a female die and then the ram (mandrel, punch, or tool) is pushed into the raw material. While the ram moves downward, the wall of the produced can moves upward, escaping through the annular gap between the ram and the die. Because the wall of the product moves upward in the direction opposite to that of the downward motion of the tool, the process

called inverse or backward extrusion. In most of the manufacturing practices involved, the product is made on a fast mechanical press; and the name "impact extrusion" has resulted.

Cold-forged parts have good surface finish and dimensional accuracy but because of higher strength of the material, cold forging requires greater forces, further the work-piece materials must have sufficient ductility at room temperature. Less ductility, micro-structural faults in original metal, wrong height/diameter ratio, incorrect die design, improper heating and lubrication, large, rapid reduction, nonuniform deformation of material etc can cause forging defects [1]. Barreling, Tears (surface cracks), edge cracks, central cavity, thermal cracks, laps, fins, wrinkles (orange peel), end grains are the defects seen in forged parts. Defects are undesirable because they reduce the strength of the forged parts which are intended to be used in critical stress applications [2]. Several ductile fracture criteria are used to predict cracks in forging. All of them need exact stress and strain values to forecast micro-crack formation. The finite element method can estimate stresses and strains to a good degree of accuracy. In the present work, an elasto-plastic FEM analysis of axisymmetric upsetting of cylindrical billet and cubical billet are carried out and damage distribution is predicted using a recently proposed continuum damage mechanics model proposed by Dhar [3,4]. And also elasto-plastic FEM analysis of back extrusion of can is carried out. Oyane's criterion [5] for ductile fracture is also considered in the study. Effect of friction at the work-die interface and size of the part, on damage, are also predicted.

1.1 Literature Review

1.1.1 Deformation Analysis of Forging Process

The problem of upsetting of metals has theoretical as well as technological significance in that its solution helps in bringing about a better understanding of the behavior of metals during plastic deformation at high pressure. It is for this reason that a number of investigators have dealt with the forging problem. Slip line solutions have been proposed by Prandtl, Hill et al. [6], and Green [7]. The slip line theory has been well developed to analyze a non-homogeneous plane strain deformation of an ideal-plastic solid. However, the elastic effect can not be incorporated and work hardening is difficult to incorporate in this method. Further, residual stresses also cannot be studied using this technique. Shabaik [8] investigated the bulging in upsetting by using the slip line theory.

Hoffman and Sach [9] proposed the slab method. A complete analysis of the slab method has been presented by Altan [10] for the axisymmetric closed die forging. In this method, a slab of infinitesimal thickness is selected and then the force equilibrium equation for the slab is written, assuming that the deformation is homogeneous within the slab and the major directions are the principal stress directions. The resulting differential equation is then solved with appropriate boundary conditions. While this method can give very good predictions of the load variation with deformation, it is inherently incapable of predicting shape changes such as barrelling in open die forging. Further, since this method is primarily based on the assumption of homogeneous deformation, it cannot predict the residual stresses as they are caused by non-uniform deformation.

The upper bound theorem was formulated by Prager and Hodge [11]. If surfaces of velocity discontinuities are included [12], then it states that among all kinematically admissible velocity fields v_i^* , the actual one minimizes the following expression

$$J^* = \int_V S_{ij}^* \dot{\epsilon}_{ij}^* + \int_{S_r} \tau |\Delta v^*| ds - \int_{S_t} T_i v_i^* ds \quad (1.1)$$

Here, $\dot{\epsilon}_{ij}^*$ is the strain rate field derived from v_i^* , S_{ij}^* is the deviatoric stress field derived from $\dot{\epsilon}_{ij}^*$ and $|\Delta v^*|$ is the discontinuity in the tangential component of the velocity across the surface S_r . Further, τ denotes the shear stress on the surface S_r and T_i is the prescribed traction on the part S_t of the boundary. The first term expresses the power spent in causing the internal deformation over the volume V of the deforming body. The second term represents the power loss over the surfaces of velocity discontinuities including the boundary between tool and material. The last term represents the power supplied by specific tractions. What the upper bound theorem states is that the actual externally supplied power is never higher than that computed by the first two terms of the above equation.

Kudo [13] applied the upper bound theorem to the problem of plane strain forging and extrusion. Kudo [14] also applied this to the analysis of axisymmetric cold forging and extrusion. McDonald et al. [15], Kobayashi [16], Avitzur [17] and many others have suggested upper bound velocity fields to predict forging load in upsetting with bulging. Yang and Kim [18], Kim et al. [19] and Manuel et al. [20] have proposed upper bound method for analysis of three-dimensional upset forging. The major difficulty in using upper bound method is how to choose a kinematically admissible velocity field since the accuracy of the solution depends on how close the assumed velocity is to actual one. Another disadvantage of the method is that the solution provided by the method does not

satisfy the equilibrium equations. So, even if elastic effects are included in integral (1.1), the method possibly cannot be used for the determination of residual stresses.

Accurate determination of forging parameters under realistic conditions became possible when the finite element method (FEM) was introduced. The major advantage of FEM is that it can be applied to a wide class of boundary value problems without restrictions on workpiece geometry. Using FEM, it is possible to predict the platen forces, the interface pressure and the stress, strain and residual stress distributions within the billet at various deformation levels.

Early applications of the FEM to forging problems were based on the incremental method proposed by Lee and Kobayashi [21]. The method uses the elastic-plastic strain matrix based on Prandtl-Reuss equations. The additivity of incremental elastic and plastic strains is assumed. Even though the stress-strain matrix and the geometry are updated after every increment, only the linearized incremental equations are used. The method was applied to solid cylinder upsetting [22], ring compression [23] and for predicting defects in upsetting [24]. Maccarini et al. [25] used the method for studying the influence of die geometry on cold extrusion forging operation. Where as Lee and Kobayashi [21] used the velocity as the primary unknown, Hartley et al. [26,27] proposed an incremental method with the displacement as the primary unknown. In Hartley's method, the linearized equations are used and the elastic plastic matrix and the geometry are updated after every increment. Shima et al. [28] proposed a rigid-plastic finite element model based on plasticity theory for porous materials. They used Coulomb's law to model the friction at the workpiece-die interface. They applied this method to upsetting of a cylinder and validated their results by conducting experiments. Three-dimensional elasto-plastic finite element analysis has been done by Pillinger et al. [29] using linearized incremental equations.

Linearized incremental equations give only an approximate solution. If the incremental size is not sufficiently small, the error between the exact and the approximate solutions grows rapidly with the applied load, as the error in the solution of the current increment gets propagated into the next increment when the stress-strain matrix and the geometry are updated. To avoid this phenomenon, non-linear incremental equations should be solved by using a scheme like Newton-Raphson technique. Such a formulation was first proposed by Bathe et al. [30]. This formulation (with or without elastic effects) has been applied to the forging problem by a few researchers. It was applied by Dadras and Thomas [31] and Carter and Lee [32] to axisymmetric upsetting.

Three dimensional rigid visco-plastic finite element analysis was done by Park and Kobayashi [33]. Surdon and Chenot [34] developed rigid visco-plastic finite element formu-

lation for the hot forging process. They considered thermal effects but did not use objective stress and strain measures. They did not consider elastic effects as the rigid-plastic/visco-plastic approach converges in fewer iterations as compared to elasto-plastic/visco-plastic approach. Fu and Luo [35] used rigid visco-plastic finite element formulation for predicting defects in isothermal forging. Terziyski et al [36] used Arbitrary Lagrangian-Eularian (ALE) FEM for three-dimensional forging. Choi et al. [37] developed three-dimensional rigid-plastic finite element formulation with special attention to treatment of the contact between the dies and work-piece.

The thrust of most of the above studies has been either to find an accurate estimation of forging load or to study deformation field. A major difficulty observed in all the previous attempts is that the increment size has to be very small in order to achieve a reasonable level of accuracy in the stress values. This leads to prohibitively large amount of computational time. The Jaumann stress measure, which is the objective stress measure used presently in the literature, does not give accurate stress values if the incremental shear deformation is large. Thus, there is a need to look for a new objective stress measure, which will allow the use of a large incremental size without compromising the accuracy of stresses. Such a measure has been recently proposed by Satyanarayana [38].

1.1.2 Deformation Analysis of Backward Extrusion

The primary operations of cold extrusion are forward extrusion, backward extrusion and radial extrusion. It is commonly accepted practice to classify extrusion operation according to the direction of material flow and the punch movement. An upper bound solutions has been given for backward-forward extrusion by Avitzur et al [39]. Later, Zhou et al. [46] stated that the deformability of backward extrusion is closely related to work hardening, anisotropy of the material at the side wall of extruded cup, and variation of inclusion morphology, etc.

Park and Hwang [48] simulated backward extrusion with a sharp cornered punch by automatic remeshing procedure. In the simulation they enforced remeshing at every deformation step. Lee, Yoon and Yang [49] proposed a systematic method for automatic renoding as a kind of weak remeshing for two dimensional and three dimensional problems, and compared with experiments carrying out for three dimensional extrusion of a square block by a cylindrical punch with a rounded corner. Shen et al. [52] proposed a method for estimating the shear friction factor in a backward extrusion-type forging. Lin and Wang [54] proposed a new upper bound elemental technique (UBET) to improve the

effectiveness of UBET for solving problems that are geometrically complex.

1.1.3 Ductile Fracture Criteria

Ductile fracture is often a limiting factor in many metal forming processes. It is well known that ductile fracture occurs due to micro-void nucleation, growth and finally coalescence into micro crack. Many ductile fracture criteria have been proposed and applied to predict ductile fracture in plastically deforming metals including metal forming processes. This section reviews some of the published ductile fracture criteria.

The published ductile fracture criteria can be broadly classified into two groups. They are

- Models based on microscopic observations about void nucleation, growth and coalescence
- Empirical and semi-empirical models

Three broad approaches have emerged which try to predict ductile fracture (micro-crack initiation) on the basis of void nucleation, growth and coalescence. They are

- Models of porous plasticity
- Models of void nucleation, growth and coalescence
- Continuum damage mechanics models

Models of Porous Plasticity

In these models, the material with voids is idealized as porous material. Thus, its constitutive equation is derived from the plastic potential of porous materials. In a porous plastic material, there is a possibility of dilatation because of which the yield surface does not remain an infinitely long cylinder like that of an incompressible material but is capped by elliptical surfaces.

Gurson's Model

Gurson [59] proposed a plastic potential function for a porous solid with randomly distributed voids of volume fraction V_f in the form

$$\Phi = \frac{\bar{\sigma}_p^2}{\bar{\sigma}^2} + 2V_f \cosh\left(\frac{3\sigma_{m_p}}{2\bar{\sigma}}\right) - (1 + V_f^2) = 0 \quad (1.2)$$

where $\bar{\sigma}_p$ and σ_{m_p} are the generalized and hydrostatic stresses of the porous aggregate and $\bar{\sigma}$ is the generalized stress of the void free (incompressible) matrix.

In this model, the growth rate of void volume fraction is considered partly due to the growth of the existing voids and partly due to the nucleation of new voids. i.e.,

$$\dot{V}_f = \dot{V}_{f-growth} + \dot{V}_{f-nucleation} \quad (1.3)$$

The rate of change of the void volume fraction due to the growth of existing voids is related to the mean strain rate $\dot{\epsilon}_{ii}$ by the relation

$$\dot{V}_{f-growth} = (1 - V_f)\dot{\epsilon}_{ii} \quad (1.4)$$

In general, void nucleation rate depends on both the generalized strain rate as well as the rate of increase of hydrostatic stress. In this model, void nucleation rate is assumed to depend only on the generalized strain rate by the relation

$$\dot{V}_{f-nucleation} = A\dot{\epsilon} \quad (1.5)$$

where A is a constant.

Gurson's criterion [59] was modified by Tvergaard [60] and Needleman and Tvergaard [61] by introducing some constant (q_1) to bring the predictions of the model into closer agreement with numerical analysis of a periodic array of voids. The modified criterion is given by

$$\Phi = \frac{\bar{\sigma}_p^2}{\bar{\sigma}^2} + 2V_f q_1 \cosh\left(\frac{3\sigma_{m_p}}{2\bar{\sigma}}\right) - (1 + (q_1 V_f)^2) = 0 \quad (1.6)$$

where q_1 is a constant.

In this model, ductile fracture is regarded as the result of an instability in the dilatational plastic flow field localized in a band (called the shear band). The fracture criterion is represented as a graph of critical localization strain versus the critical void volume fraction with strain hardening exponent as a parameter.

Oyane's Model

Oyane [5] and Oyane et al. [62] used the plasticity theory for porous materials to propose a ductile fracture criterion indicating that micro crack initiates whenever the volumetric strain reaches a material dependent critical value. For pore free materials, assuming that the material obeys porous plasticity equations after the initiation of voids, Oyane obtained

the criterion for ductile fracture as

$$\int_0^{\epsilon_{vf}} f_\rho^2 \rho_r^{2n-1} d\epsilon_v = C \quad (1.7)$$

where f_ρ is a function of relative density ρ_r which is defined as the ratio of the apparent density of the porous material to the density of the pore free matrix, ϵ_{vf} is the volumetric strain at fracture and n and C are constants. The constant C is given by

$$\int_{\bar{\epsilon}_i}^{\bar{\epsilon}_f} \left(1 + \frac{\sigma_m}{A\bar{\sigma}}\right) d\bar{\epsilon} = C \quad (1.8)$$

where $\bar{\epsilon}_i$ is the generalized strain at which voids get initiated, $\bar{\epsilon}_f$ is the generalized strain at which fracture occurs and A is a material constant. By assuming that $\bar{\epsilon}_i = 0$, the above criterion reduces to a simple form

$$\int_0^{\bar{\epsilon}_f} \left(1 + \frac{\sigma_m}{A\bar{\sigma}}\right) d\bar{\epsilon} = C \quad (1.9)$$

For porous materials, they modified the criterion by including the relative density term into the integral. Thus,

$$\int_0^{\bar{\epsilon}_f} \left(1 + \frac{\sigma_m}{A\rho_r^n \bar{\sigma}}\right) d\bar{\epsilon} = C\rho_0 B \quad (1.10)$$

Here $\rho_r^n \bar{\sigma}$ is the generalized flow stress of the porous material, B is a constant and ρ_0 is the initial relative density of the porous material. A method for estimating values of the material constants using the compression test has been provided by them.

The major limitation of the above two criterion is that they do not model ductile fracture (i.e., micro-crack initiation) as a void coalescence phenomenon.

Models of Void Nucleation, Growth and Coalescence

The void nucleation model of Goods and Brown [63], the void growth models of McClintock [64] and Rice and Tracey [65] and void coalescence model of Thomason [96] along with some additional models on void nucleation and growth are discussed in this section.

Models of Void Nucleation

Goods and Brown [63] developed a stress based void nucleation model based on the condition that the voids nucleate by decohesion of particles whenever the normal stress reaches a critical value (σ_c) at the particle/matrix interface. They obtained a relation between the void nucleation strain (ϵ_1^n) and hydrostatic stress (σ_m) as

$$\epsilon_1^n = Kr_p(\sigma_c - \sigma_m)^2 \quad (1.11)$$

where K is a material constant dependent on the particle volume fraction and r_p is the particle radius. Experiments on Fe-Fe₃C system [63] confirm the linear relationship between the nucleation strain and particle radius. This relation is for small spheroidal particles of radius less than or equal to 1 μ m.

For large size particles, the approximate analysis of Argon and Im [66] gives the condition for the void nucleation by decohesion as

$$\bar{\sigma} + \sigma_m = \sigma_c \quad (1.12)$$

For a given problem, this condition can be expressed in terms of the nucleation strain. Note that this relation is independent of particle radius.

Gurland [67] proposed a nucleation model based on the experiments conducted by him on 1.05% C spheroidal steel. Experimental observations reveal that the void nucleation occur by cracking of cementite particles. Voids nucleate at all strain levels depending on the size, shape and orientation with the maximum principal stress direction. It is observed that the volume fraction of broken particles is a linear function of the plastic strain.

Void Growth Models

Once the nucleation of micro-voids takes place either by decohesion or cracking of a secondary particle or inclusion, the resulting stress free surface of the void produces a localized stress and strain concentration in the plastically surrounding matrix. With continuing plastic flow of the matrix, the void undergoes volumetric growth and change of shape. Some of the published void growth models are discussed here.

McClintock [64] proposed a void growth model for two-dimensional plane strain problems considering a single elliptic void. He assumed that the major and minor axes of the void coincide with the principal stress directions. He obtained the following closed form expression for void growth in a rigid work-hardening material whose generalized stress-strain

relation is $\bar{\sigma} = K\bar{\epsilon}^n$:

$$\ln \frac{R_h}{R_{0h}} = \frac{\sqrt{3}\bar{\epsilon}}{2(1-n)} \sinh \frac{\sqrt{3}(1-n)}{2} \frac{\sigma_a + \sigma_b}{\bar{\sigma}} + \frac{\epsilon_a + \epsilon_b}{2} \quad (1.13)$$

where R_h and R_{0h} are the current and initial mean radii of the hole respectively, σ_a and σ_b are the principal stresses and ϵ_a and ϵ_b are the principal strain components along the major and minor axes respectively. Fracture was assumed to occur at the point where a growing void touches the cell boundary. Dung [68,69] modified and extended McClintock's model [64] to analyze the growth of circular/elliptic voids in plane strain problems and spherical/ellipsoidal voids in three-dimensional problems.

Rice and Tracey [65] considered a single spherical void of initial radius R_{0v} in a remote uniform strain rate field $\dot{\epsilon}_{ij}$ and remote stress field σ_{ij} in a rigid plastic material. They obtained the following expression for the rate of change of the radii (\dot{R}_{kv}) of the void in the principal strain rate directions:

$$\dot{R}_{kv} = \{(1+F)\dot{\epsilon}_k + \dot{\epsilon}H\}R_{mean} \quad (1.14)$$

where

$$\begin{aligned} F &= \frac{2}{3} \text{ for linear hardening and for low values of } \sigma_m \text{ for non hardening} \\ &= 1 \text{ for high values of } \sigma_m \text{ for non hardening} \\ H &= 0.75 \frac{\sigma_m}{\bar{\sigma}} \text{ for linear hardening} \\ &= 0.558 \sinh \frac{3}{2} \frac{\sigma_m}{\bar{\sigma}} + 0.008\nu \cosh \frac{3}{2} \frac{\sigma_m}{\bar{\sigma}} \text{ for non hardening,} \end{aligned}$$

$$R_{mean} = \frac{1}{3} (R_{1v} + R_{2v} + R_{3v})$$

$$\dot{\epsilon} = \text{generalized strain rate}$$

$$\begin{aligned} \dot{\epsilon}_k &= \text{principal strain rates} \\ &= -\frac{3\dot{\epsilon}_2}{\dot{\epsilon}_1 - \dot{\epsilon}_3}, \text{ Lode variable.} \end{aligned}$$

Note that an initial spherical void grows into an ellipsoidal void of principal radii R_{1v} , R_{2v} and R_{3v} . Thomason [96] integrated the above equation by assuming that the principal axes of strain rates remain fixed in direction throughout the strain path and obtained the

following expressions for the principal radii of the void:

$$R_{1v} = \left(A + \frac{3B(1+\nu)}{2\sqrt{\nu^2+3}} \right) R_{0v} \quad (1.15)$$

$$R_{2v} = \left(A - \frac{\nu B}{\sqrt{\nu^2+3}} \right) R_{0v} \quad (1.16)$$

$$R_{3v} = \left(A + \frac{(\nu-3)B}{2\sqrt{\nu^2+3}} \right) R_{0v} \quad (1.17)$$

where

$$A = \exp \frac{2\sqrt{\nu^2+3}}{3+\nu} H \epsilon_1^g$$

$$B = \frac{1+F}{H} (A-1)$$

and ϵ_1^g is the integral of the largest principal strain rate. Thomason [96] used the above expressions in the derivation of the void coalescence condition.

For an array of void nucleating particles of diameter D_p and spacing d_s , setting the initial void radius as $D_p/2$, eqns. (1.13) and (1.14) leads to the following expression for fracture strain:

$$\bar{\epsilon}_f = \frac{\ln(d_s/D_p)(1-n)}{\sinh[(1-n)(\sigma_a + \sigma_b)/(2\bar{\sigma}/\sqrt{3})]} \quad [\text{McClintock}] \quad (1.18)$$

$$\bar{\epsilon}_f = \frac{\ln(d_s/D_p)}{0.28 \exp(1.5\sigma_{kk}/\bar{\sigma})} \quad [\text{Rice and Tracey}] \quad (1.19)$$

Some research workers have used the above expressions for the prediction of ductile fracture with the help of experimentally determined parameters. The major limitations of this approach are that it ignores the effects of void nucleation (as the expressions are derived from a pre-existing finite size void) and void coalescence. Thus, $\bar{\epsilon}_f$ is usually overestimated.

Void Coalescence Model

Thomason [96] modeled void coalescence phenomenon as plastic instability due to necking of the inter void matrix. The sufficient condition for plastic instability of the inter-void matrix, as given by him, is

$$\sigma_n \bar{A}_n - \sigma_1 = 0 \quad (1.20)$$

where \bar{A}_n is the area fraction of the inter-void matrix perpendicular to the direction of maximum principal stress σ_1 and σ_n is the plastic constraint stress. He considered a

geometrically equivalent square prismatic void and used the upper bound method to obtain an expression for the plastic constraint stress in terms of the void dimensions, inter-void spacing and the yield stress.

Thomason's Fracture Criterion

Thomason [96] combined the results of Goods and Brown [63] on void nucleation, Rice and Tracey [65] on void growth and his own on void coalescence to arrive at a fracture criterion. He used expressions (1.15 to 1.17) for the void dimensions to express the void coalescence condition (eqn. 1.20) in terms of the void growth strain ϵ_1^g and the hydrostatic stress σ_m . By superposing this condition on the void nucleation relation (eqn. 1.11), he obtained the fracture criterion as a graph of fracture strain ($\bar{\epsilon}_f = \epsilon_1^n + \epsilon_1^g$) versus the triaxiality (i.e., the ratio of hydrostatic stress to the generalized stress).

The main drawback of this approach is the use of expressions (1.15 to 1.17) for void growth. These expressions are based on integration procedure which assumes that the principal directions of strain rate remain fixed throughout the strain path. This is, in general, true only for the case of small strain and rotation. As a result, this approach cannot be used when the strains and/or rotations are large.

Continuum Damage Mechanics Models

In these models, material behavior is represented by a plastic potential which includes damage as an internal variable. The damage variable quantifies the intensity of voids, which can be identified as either the void volume fraction or the area void fraction. The basis of continuum damage mechanics models rests on the theory of continuum thermodynamics. In this section some of the continuum damage mechanics models are discussed.

Lemaitre [70] proposed a continuum damage mechanics model for void growth in elastoplastic materials with area void fraction as the damage variable using the concepts of effective stress and strain equivalence. His model is based on a simple damage growth law in which the damage rate is linearly dependent on the plastic strain and the thermodynamic force corresponding to the damage. It does not account for void nucleation. Note that, as far as void coalescence is concerned, it has to be incorporated as an additional condition in terms of the continuum parameters. This condition, which serves as a fracture criterion, has to be based on an appropriate micro model. Thomason's limit load model seems to be a good candidate for this purpose.

More recently Dhar [4] and Dhar et al. [3] extended Lemaitre's [70] continuum damage

mechanics model to incorporate a damage growth law which accounts for both the void nucleation as well as void growth. The law is based on the experimental results of Le Roy et al. [71]. They also modified Thomason's [96] void coalescence condition to make it suitable for the case of large strain and/or rotation. They combined the extended continuum damage mechanics model and modified void coalescence condition to arrive at a criterion for prediction of micro crack initiation. The salient features of the above approach are discussed below.

In this model, damage D is identified as an area void fraction at a point in a plane. Thus, it is defined by

$$D = \frac{\Delta A_v}{\Delta A} \quad (1.21)$$

where ΔA is the infinitesimal area around the point in some plane and ΔA_v is the area of the voids in the plane containing ΔA . The conjugate variable corresponding to D is $-Y$, the rate at which the elastic energy releases during the damage growth at constant stress. For an isotropic material, $-Y$ is given by [70]

$$-Y = \frac{\bar{\sigma}^2}{2E(1-D)^2} f\left(\frac{\sigma_m}{\bar{\sigma}}\right) \quad (1.22)$$

where

$$f\left(\frac{\sigma_m}{\bar{\sigma}}\right) = \frac{2(1+\nu)}{3} + 3(1-2\nu) \left(\frac{\sigma_m}{\bar{\sigma}}\right)^2 \quad (1.23)$$

Here, E is the Young's modulus, ν is the Poisson's ratio and $(\sigma_m/\bar{\sigma})$ is called the triaxiality. The damage growth law is given by

$$\dot{D} = C_D \dot{\epsilon} + (a_1 + a_2 D) (-Y) \dot{\epsilon} \quad (1.24)$$

where a_1 , a_2 and C_D are material constants. Here the first term, which is independent of $-Y$, represents the damage evolution due to void nucleation while the second term, which is dependent on $-Y$, represents the evolution of damage due to void growth. For AISI 1090 steel, Dhar et al. [3] determined the constants fitting eqn. (1.23) through the experimental results of Le Roy et al. [71]. They obtained the following values:

$$\begin{aligned} C_D &= 1.898 \times 10^{-2} \\ a_1 &= 9.8 \times 10^{-4} \text{ MPa}^{-1} \\ a_2 &= 1.84 \text{ MPa}^{-1} \end{aligned}$$

While getting these constants, they used Bridgman's relation [72] to express the triaxiality as a function of strain.

Dhar et al. [3] used finite strain expressions for the void dimensions and inter-void spacing to express Thomason's void coalescence criterion (eqn. 1.19) in the following form:

$$\sigma_1 \left[0.1 + \frac{1.2}{\{1 - \exp(-\bar{\epsilon}/2)\}^{0.5}} \right] \exp(-\bar{\epsilon}) \bar{\sigma} = 0 \quad (1.25)$$

where $\bar{\epsilon}$, the generalized strain, is the integral of $\dot{\bar{\epsilon}}$ along the path lines. To find the critical value of damage parameter (D_c), they applied this criterion to various geometries and loading conditions using the elasto-plastic finite element analysis. They observed that D_c is independent of geometry or loading and hence that can be used as a material property for the prediction of micro-crack initiation. They reported that the value of D_c is 0.05 for AISI 1090 steel.

Empirical and Semi-Empirical Models

In the absence of reliable quantitative models for incorporating the phenomena of void nucleation, growth and coalescence in materials undergoing large plastic deformation in metal forming processes, many empirical relations based on some phenomenological models have been proposed. This section reviews some of them.

Freudenthal [73] postulated that generalized plastic work per unit volume is the critical parameter and is expressed as

$$\int_0^{\bar{\epsilon}_f} \bar{\sigma} d\bar{\epsilon} = C_1 \quad (1.26)$$

Cockcroft and Latham [74] modified the generalized plastic work criterion to take care of the effects of change in the neck geometry which is observed in tensile tests. The criterion is given by

$$\int_0^{\bar{\epsilon}_f} \bar{\sigma} \frac{\sigma_1}{\bar{\sigma}} d\bar{\epsilon} = \int_0^{\bar{\epsilon}_f} \sigma_1 d\bar{\epsilon} = C_2 \quad (1.27)$$

Here σ_1 is the maximum normal stress.

Oh et al. [24] modified Cockcroft and Latham criterion [74] by considering the ratio of the maximum tensile stress to the generalized stress. This criterion is expressed as

$$\int_0^{\bar{\epsilon}_f} \frac{\sigma_1}{\bar{\sigma}} d\bar{\epsilon} = C_3 \quad (1.28)$$

The main drawback of the above three criteria is that the effect of hydrostatic stress is not considered. Osakada and Mori [75] developed a ductile fracture criterion which

includes the effects of both plastic strain and hydrostatic stress and expressed it as

$$\int_0^{\bar{\epsilon}_f} < a + \bar{\epsilon} + b\sigma_m > d\bar{\epsilon} = C_4 \quad (1.29)$$

$$< \bullet > = \bullet \quad \bullet \geq 0$$

$$< \bullet > = 0 \quad \bullet < 0$$

where a and b are material constants.

Norris et al. [76] developed a fracture criterion based on their experimental results and finite difference results of several test geometries and expressed it as

$$\int_0^{\bar{\epsilon}_f} \frac{1}{(1 - C\sigma_m)} d\bar{\epsilon} = C_5 \quad (1.30)$$

where C is a constant.

In the above equations C_1, \dots, C_5 are the critical values accumulated over the strain path to fracture.

1.1.4 Defects in Forging

Different types of defects are observed in industrial metal forming processes, which have been tabulated by Johnson and his co-workers [81,86,88]. Later Arentoft and wanheim classified defects into six groups: folds, shear defects, cracks, form defects and structural defects. He reported that the limit of forming processes is governed by the material structure, friction, height to diameter ratio, temperature, rate of deformation and geometry. It is a well-established fact that the tensile triaxiality is the main factor contributing to the fracture initiation in these processes.

There are mainly two defects in open die forging namely barreling and cracks. Barreling occurs due to friction between the part and the die or when there is a large temperature difference between the part and the die. This leads to greater deformation in the midsection of the part than at the constrained ends [80]. The amount of barreling is more for unlubricated conditions [78].

In simple upsetting, ductile fracture occurs at the barreled surface and the condition of fracture depends on the complete history of the plastic flow.

Thomason's [77] uniaxial compression test results support the hypothesis that a metal must reach a state of tensile plastic instability before ductile fracture, by the nucleation,

growth and coalescence of internal microscopic cavities can begin. He observed ductile fracture occurred on the surface of uniaxial compression specimens without any evidence of external local necking.

Kuhn and Lee [79] conducted experiments on steel cylinders under varying conditions. A refined measurements of strains revealed that the axial strain suddenly reached a plateau and remained constraint while the hoop strain continued to increase. The axial strain then resumed its increase and did so at the same rate as the hoop strain. They interpreted this strain perturbation as a localized instability in strain and hence localized necking of material, between inhomogeneities, which eventually led to fracture. Also they metallographically detected void formations prior to fracture.

Osakada and Mori [75] conducted experiments on carbon steel. From the metallographic observations, he reported that ductile fracture Will occur due to formation of fracture-nuclei (voids) at the inclusion sites after a certain amount of plastic strain, the growth of the fracture-nuclei with continuing plastic strain and coalescence or rapid growth of the nuclei for macroscopic fracture due to strain concentration within narrow bands. These stages are affected by the hydrostatic stress component, and thus the fracture increases with the increase in environmental pressure.

Sowerby, Dung et al. examined the capability of McClintock's void growth model to predict damage accumulation in the upsetting of steel specimens using rigid-plastic formulation and found it appropriate for homogeneous metals [82,84]. Predeleanu et al. [85] conducted experiments and computer simulations using their damage criterion and found that material damage reaches a critical value inside the specimen and not at the free surface. They also detected voids and micro-cracks within the interior of the specimen before surface fracture.

Clift et al. [87,83] used 3-D elasto-plastic Finite element analysis using eight noded brick element. They modeled boundary friction conditions by defining an extra layer of elements, referred to as the friction layer on the required surfaces. But they didn't report effect of friction in their study.. The numerical results were used to give predictions of fracture initiation site for a total of nine fracture criteria. They compared these predicted sites with experiments and showed that generalized plastic work per unit volume criterion , is capable of estimating the experimental fracture initiation sites for the complete range of processes considered. They re-confirmed that the fracture criterion proposed by Ghosh was not successful in any one of the cases examined [83,87].

Zhu et al. [89,91] also disapproved Ghosh criterion in their simulation on side pressing of cylindrical billets.

Lin and Lin [90] used strain energy density failure criterion in conjunction with coupled thermo-elastic-plastic large deformation model to analyze ductile fracture in upsetting of the cylindrical specimen under various geometrical and frictional conditions. They reported increased damage with higher friction.

Semiatin et al. [94] conducted hot forging trials on Ti-6Al-4V specimens and validated the results with Finite element analysis and suggested that the Rice and Tracey void growth model which highlights that the influence of hydrostatic stress and Cockcroft and Latham criterion provided good estimate of surface fracture.

Atkins [92] reported that well lubricated cylinders developed inclined cracks found in shear while unlubricated ones showed vertical cracks formed in tension. He also mentioned that the greatest strains to fracture occur at the least values of hydrostatic stress.

Recently, Kim et al. [95] investigated the ductile fracture criterion based on work hypothesis and Cockcroft and Latham criterion, and carried out experiments and rigid-viscoplastic finite element analysis studies on simple upsetting of aluminum billets. They deduced that Cockcroft and Latham's criterion gave a more reasonable prediction for crack initiation site than work hypothesis and the former was useful in processes like cold forging in which the influence of the induced circumferential tensile stress on failure is dominant.

Gouveia et al. [93] used finite element analysis and experimental results to analyze four ductile fracture criteria in forging. They reported Freundenthal criterion predicted much higher values of damage inside the specimen and thus located fracture initiation site at the center of the billet. The drawback of Cockcroft-Latham criterion, they suggested, was if the largest principal stress σ_1 is temporarily negative led to accumulation of negative damage. They concluded that the Oyane's criterion which is formulated on the basis of the void growth model and the theory of the plasticity of the porous media, was the best among the criteria considered.

1.2 Scope and Objective of the Present Work

Literature review reveals that there have been few attempts to predict the crack occurrence in bulk metal forming processes. Ductile fracture in metal forming processes is established as a void nucleation, growth and coalescence phenomenon. Dhar et al. [3] combined the continuum damage mechanics model of Lemaitre [70] with the void coalescence criterion of Thomason [96] to propose a criterion for micro-crack initiation in terms of the critical value of the damage parameter. This criterion incorporates all the features of microscopic description of ductile fracture, namely void nucleation, growth and coalescence. This

criterion is taken to predict damage distribution in a AISI-1090 workpiece. Present work aims at prediction of crack in various bulk metal forming processes by choosing the proper process variables through finite element based process.

The main objective of the present work is to predict the micro-crack initiation in axisymmetric, three dimensional upsetting and backward extrusion process. In the present work, user defined programs (modules) are added to DEFORM-3D software to obtain the damage distribution in bulk metal forming processes. These programs are used to predict the damage distribution based on critical damage criterion of Dhar et al. and Oyane's criterion. A detailed parametric study of damage and hydrostatic stress distribution are carried out to show the effect of coefficient of friction and geometric ratios (height to diameter, or height to width ratio, width to thickness ratio) of the work piece.

The damage distribution in backward extrusion process is studied by using Cockcroft and Latham criterion. A detailed parametric study is carried out to show the effect of the punch nose face angle on damage distribution. Convergence study is carried out.

1.3 Organization of Thesis

The thesis is organized as follows. In the second chapter, modeling of objects, boundary conditions and formulation of ductile fracture criteria are presented. In the third chapter, results for a typical case are presented. It also includes a discussion on parametric study. Conclusions and suggestions for future work are presented in chapter 4.

Chapter 2

FORMULATION

In the present work DEFORM-3D (*Design Environment for FORMing-3 Dimensional*) software is used to predict the micro-crack initiation in the bulk metal forming operations. Routines required to predict damage are added as an external routines during post processing stage.

A brief description of the DEFORM software is presented in section 2.1 along with the procedure of adding external routines. Object geometries and the boundary conditions chosen for varying problems selected in the present study are given in section 2.2. The implementation procedure of three fracture criteria considered in the present work to predict the damage in the bulk metal forming processes is presented in section 2.3.

2.1 Introduction

DEFORM is a Finite Element Method (FEM) based process simulation system designed to analyze various bulk metal forming processes. Unlike general purpose FEM codes, DEFORM is tailored for deformation modeling. DEFORM consists of extensive material data base for many common alloys including steels, aluminums and super-alloys. In addition user defined material properties can be given as input. Deform software has provision to add user defined subroutines for material modeling, punch movement modeling, fracture criteria etc.

DEFORM software is developed using Updated Lagrangian formulation. In this formulation, it is assumed that the states of stress and deformation of the body are known till the current configuration, say at time t . The main objective is then to determine the incremental deformation and stresses during an infinitesimal time step, Δt , i.e from time t to

$t+\Delta t$. Here, the current configuration is used as the reference configuration for obtaining the incremental values. Unlike in the Lagrangian formulation, an incremental strain tensor is used. This methodology is particularly useful for elasto-plastic materials because the stress-strain relationship in such materials is usually expressed in an incremental fashion.

2.2 DEFORM - An Introduction

The DEFORM system consists of three major components:

- A pre-processor for creating, assembling, or modifying the data required to analyze the simulation, and for generating the required database files.
- A simulation module for performing the numerical calculations required to analyze the process, and writing the results to the database file. The simulation module reads the database file, performs the actual solution calculation, and appends the appropriate solution data to the database file.
- A post-processor for reading the database file from the simulation module and displaying the results graphically and for extracting numerical data.

2.2.1 Object Modeling

The DEFORM software is having the facility to import the solid models of the specified formats. Those are STL, AMGGEO, PARTRAN and I-DEAS. Out of these I-DEAS is chosen. The following phases of the various modules available in I-DEAS are used in the present work.

Simulation: Modeling
 Meshing

Different parts like cubical, one fourth of cylindrical workpieces and punch are considered in modeling. In meshing phase two different elements are used, brick element being used for a cubical work piece and tetrahedron element being used for upsetting of a cylindrical workpiece and backward extrusion. Uniform meshing style is used for all the parts.

This meshing model is exported to DEFORM-3D using universal file format. It stores nodes, corresponding nodal coordinates, elements and their connectivity.

2.2.2 Adding user defined programs

The FEM user defined routines can be used for many different purposes during a simulation. To implement the user routines, FORTRAN 77 compiler must be installed in the system. In this software, user defined programs can be added to pre-processor and post-processor.

User defined pre-processing routines: The user defined pre-processing routines have to be written with in the file named DEF_USR.FOR. In this software, there is a provision to write user defined routines for flow stress definition, movement control and adding two nodal and elemental variables.

User defined post-processing routines: The user defined post-processing routines have to be written in the PSTUSR3.FOR file. User defined post-processing routines can be used to generate plots of user variables after obtaining the results. It uses the results that are stored in the database and any variable can be plotted in the post-processor. In this software, 10 user defined routines can be implemented, and each of these can be used to calculate 20 different user variables. When user variable tracking is done the functions in this FORTRAN program are called for the results that have been selected in the post-processor. The user function is evaluated at each node/element of the object for which the variables are tracked. The user subroutine is called at the beginning of tracking to get the variable names, then at the first step to get the initial values for all variables and then called for all the steps present in the database being tracked. There are three phases in the tracking process:

Phase 1:

- The user variable function is called with the INIT flag set to "0". This is done once before tracking is started. During this phase the variables names (VNAME) should be defined so that they can be displayed in plots on the screen. The variables for which "VNAME" is defined are tracked.

Phase 2:

- The user variable function is then called with INIT flag set to "1". This is the second phase in which all user variables have to be initialized to their starting values. This

is called at the first step in the list of steps which are being tracked (ISTEP equals to the starting step) for each node/element in the object.

Phase 3:

- In this phase, all the user variables are calculated and assigned to the corresponding user variables. If a remeshing step has been purged from a database then user-variable tracking will not work with the database.

Compile and execution of user defined programs : Copy all the files of DEFORM's /USR and /EXE directories to a local directory. In case of pre-processor routine replace the DEF_USR.FOR file with modified DEF_USR.FOR. Using the command script DEF_INS.COM, compile and link the new DEF_SIM.EXE. Run DEFORM 3D pre-processor and generate the database file. Change the the data base file name to FOR003 and run the DEF_SIM.EXE. Load the database file(FOR003) in the DEFORM post and get the results. If the program is post-processor routine, replace the PSTUSR3.FOR file with new PSTUSR3.FOR file. Using the command script DEF_INS.COM, compile and link the new DEF_SIM.EXE. Load the database file and get the results.

2.3 Boundary Conditions

2.3.1 Upsetting of Cylindrical Workpiece

Figure 2.1 shows the domain of the problem. Due to symmetry only one-eighth part of the block is used for analysis. The boundary conditions used in the present work are given below. for the domain of this problem are discussed below.

X-Y Plane of Symmetry (Plane DEF)

Because of plane of symmetry, material flow perpendicular to X-Y plane (i.e. in Z-axis direction) is zero. Therefore the incremental displacement at the nodes lying on that plane DEF in Z-axis direction is zero.

$$\text{i.e., } \Delta U_z = 0$$

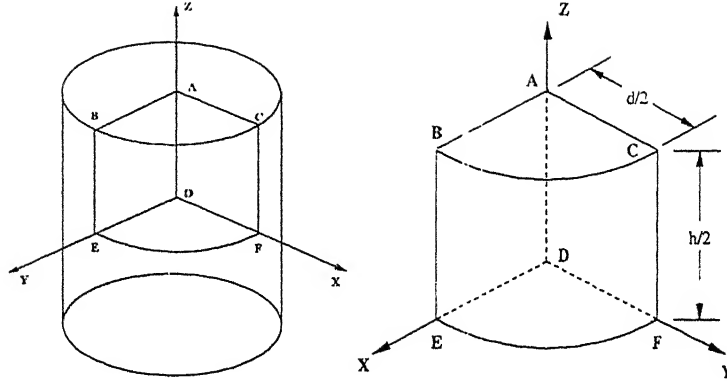


Figure 2.1: Domain for cylindrical workpiece forging

Y-Z Plane of Symmetry (Plane ACFD)

Because of symmetry, material flow perpendicular to Y-Z plane (i.e. in X-axis direction) is zero. Therefore the incremental displacement at the nodes lying on that plane ACFD in X-axis direction is zero.

$$\text{i.e., } \Delta U_x = 0$$

X-Z Plane of Symmetry (Plane ABED)

Because of symmetry, material flow perpendicular to X-Z plane (i.e. in Y-axis direction) is zero. Therefore the incremental displacement at that nodes lying on the plane ABED in Y-axis direction is zero.

$$\text{i.e., } \Delta U_y = 0$$

2.3.2 Upsetting of Cubical Workpiece

Figure 2.2 shows the domain of the problem. Due to symmetry only one-eighth part of the block is used for analysis. The boundary conditions used in the present work is presented below.

X-Y Plane of Symmetry (Plane CDHG)

Because of plane of symmetry, material flow perpendicular to X-Y plane (i.e. in Z-axis direction) is zero. Therefore the incremental displacement at the nodes lying on that plane CDHG in Z-axis direction is zero.

$$\text{i.e., } \Delta U_z = 0$$

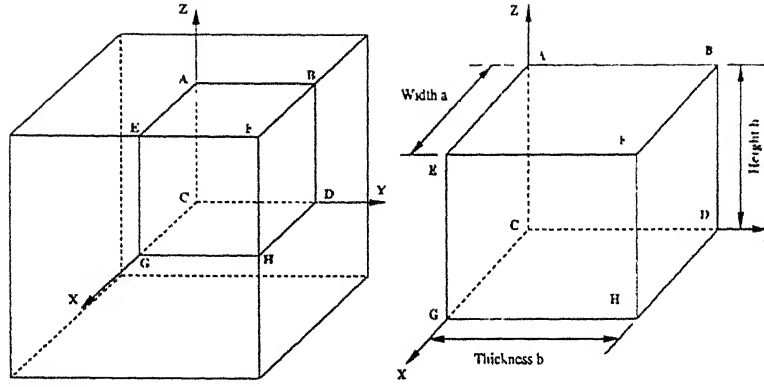


Figure 2.2: Domain used for cubical workpiece upsetting

Y-Z Plane of Symmetry (Plane ABDC)

Because of symmetry, material flow perpendicular to Y-Z plane (i.e. in X-axis direction) is zero. Therefore the incremental displacement at the nodes lying on that plane ABDC in X-axis direction is zero.

$$\text{i.e., } \Delta U_x = 0$$

X-Z Plane of Symmetry (Plane ACGE)

Because of symmetry, material flow perpendicular to X-Z plane (i.e. in Y-axis direction) is zero. Therefore the incremental displacement at that nodes lying on the plane ACGE in Y-axis direction is zero.

$$\text{i.e., } \Delta U_y = 0$$

2.3.3 Backward Extrusion of a cylindrical workpiece with cylindrical punch

Figure 2.3 shows the domain of the problem. Due to symmetry only one-fourth part of the block is used for analysis. The boundary conditions used in the present work is given below.

Y-Z Plane of Symmetry (Plane ABED)

Because of symmetry, material flow perpendicular to Y-Z plane (i.e. in X-axis direction) is zero. Therefore the incremental displacement at the nodes lying on that plane ABED in X-axis direction is zero.

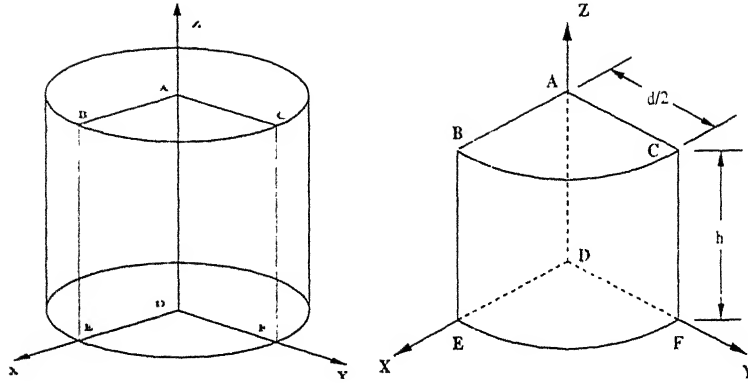


Figure 2.3: Domain used for backward extrusion

i.e., $\Delta U_x = 0$

X-Z Plane of Symmetry (Plane ACFD)

Because of symmetry, material flow perpendicular to X-Z plane (i.e. in Y-axis direction) is zero. Therefore the incremental displacement at that nodes lying on the plane ACFD in Y-axis direction is zero.

i.e., $\Delta U_y = 0$

2.4 Implementation Procedure of Ductile Fracture Criteria

A critical damage criterion proposed by Dhar [3,4] is used to predict micro-crack initiation in the upsetting of cylindrical and cubical workpiece. Oyane's criterion [5,62] is used to predict micro-crack initiation in upsetting of cylindrical workpiece only and the Cockcroft and Latham criterion [74] is used in case of backward extrusion.

2.4.1 Critical Damage Criterion [Dhar et al.]

In this model, damage D is identified as an area void fraction at a point in a plane. It is defined by equation (1.21)

The damage growth law which gives rate of change of D is given by equation (1.24), which is reproduced below:

$$\dot{D} = C_D \dot{\epsilon} + (a_1 + a_2 D) (-Y) \dot{\epsilon} \quad (2.1)$$

where $-Y$ is the rate at which the elastic energy releases during the damage growth at constant stress. For an isotropic material, it is given by [70]

$$-Y = \frac{\bar{\sigma}^2}{2E(1-D)^2} f\left(\frac{\sigma_m}{\bar{\sigma}}\right) \quad (2.2)$$

where

$$f\left(\frac{\sigma_m}{\bar{\sigma}}\right) = \frac{2(1+\nu)}{3} + 3(1-2\nu) \left(\frac{\sigma_m}{\bar{\sigma}}\right)^2 \quad (2.3)$$

As already described in section 1.2.3, the constants fitting equation (2.1) are found for AISI 1090 steel as:

$$C_D = 1.898 \times 10^{-2}, a_1 = 9.8 \times 10^{-4} \text{ MPa}^{-1} \text{ and } a_2 = 1.84 \text{ MPa}^{-1}.$$

For an increment, eqn. (2.1) can be written to give the value of D at a point in the domain as

$${}_t\Delta D = C_D {}_t\Delta \bar{\epsilon} + (a_1 + a_2 {}_tD) (-{}^{t+\Delta t}Y) {}_t\Delta \bar{\epsilon} \quad (2.4)$$

where

$$-{}^{t+\Delta t}Y = \frac{{}^{t+\Delta t}\bar{\sigma}^2}{2E(1-{}_tD)^2} f\left(\frac{{}^{t+\Delta t}\sigma_m}{{}^{t+\Delta t}\bar{\sigma}}\right) \quad (2.5)$$

where function f is as defined in equation (2.3).

Since, the strains and stresses are calculated at the Gauss points, value of ΔD can be found at every Gauss point in an element. This can then be used to determine damage growth variable D at time $t + \Delta t$. The value of D should be taken as zero at the beginning.

$${}^{t+\Delta t}D = {}_tD + {}_t\Delta D \quad (2.6)$$

Thus, a damage distribution in the domain can be obtained. The crack initiates where ever the value of D reaches the critical limit of 0.05 (for AISI 1090 steel).

2.4.2 Oyane's Criterion

A variable D_{oy} is used to denote damage predicted by Oyane's criterion. Recalling Oyane's equation (1.9) for pore free materials, this can be given as

$$D_{oy} = \int_0^{\bar{\epsilon}} \left(1 + \frac{\sigma_m}{A\bar{\sigma}}\right) d\bar{\epsilon} \quad (2.7)$$

where the constant $A = 0.24$ for UNI-3571 aluminum alloy.

The incremental D_{oy} at time t can be given as

$${}_t\Delta D_{oy} = \left(1 + \frac{{}^{t+\Delta t}\sigma_m}{A {}^{t+\Delta t}\bar{\sigma}}\right) {}_t\Delta \bar{\epsilon} \quad (2.8)$$

Initially, the value of damage should be taken as zero and then damage at time $t + \Delta t$, ${}^{t+\Delta t}D_{oy}$ can be evaluated at a point in the domain in each increment as

$${}^{t+\Delta t}D_{oy} = {}^tD_{oy} + {}_t\Delta D_{oy} \quad (2.9)$$

Knowing the stresses and strains, the value of D_{oy} is found at every Gauss point in the domain and Oyane's damage distribution is found. The crack starts at the point where the value of D_{oy} crosses the critical limit of 0.348 (for UNI-3571).

2.4.3 Cockcroft and Latham criterion

Cockcroft and Latham [74] modified the generalized plastic work criterion to take care of the effects of change in the neck geometry which is observed in tensile tests. The criterion is given by

$$\int_0^{\bar{\epsilon}_f} \bar{\sigma} \frac{\sigma_1}{\bar{\sigma}} d\bar{\epsilon} = \int_0^{\bar{\epsilon}_f} \sigma_1 d\bar{\epsilon} = C_2 \quad (2.10)$$

Here σ_1 is the maximum normal stress.

The incremental C_2 at time t can be given as

$${}_t\Delta C_2 = \sigma_{1t} \Delta \bar{\epsilon} \quad (2.11)$$

Initially, the damage value is zero and at time $t + \Delta t$ the damage ${}^{t+\Delta t}C_2$ can be evaluated at a point in the domain in each increment as

$${}^{t+\Delta t}C_2 = {}^tC_2 + {}_t\Delta C_2 \quad (2.12)$$

Chapter 3

RESULTS AND DISCUSSION

The finite element analysis of 3-dimensional forging and backward extrusion is studied for various sets of input variables.

In this chapter, the study is performed on forging and backward extrusion operations. Only one-eighth of the block is considered for forging analysis due to symmetry about X, Y and Z directions. For backward extrusion one-fourth of the block is considered due to symmetry about X and Y directions. The convergence is checked for the damage variable D and hydrostatic stress. In section 3.1.1, some typical results are presented for cylindrical workpiece where growth of Dhar's damage variable D is discussed along with the hydrostatic stress and circumferential stress σ_θ distributions. In section 3.1.2, the Dhar's damage variable D is discussed for cubical workpiece. The parametric study is carried out to show the effect of various input variables for both the cases.

In section 3.2, some typical results are presented for cylindrical workpiece, where growth of Oyane's damage variable D_{oy} is discussed along with the hydrostatic stress and circumferential stress distributions. The parametric study for cylindrical workpiece is also presented to show effect of various input variables.

In section 3.3, results are discussed for backward extrusion. In this section Cockcroft and Latham damage C_2 is discussed with the hydrostatic stress. The effect of punch nose face angle in backward extrusion is studied.

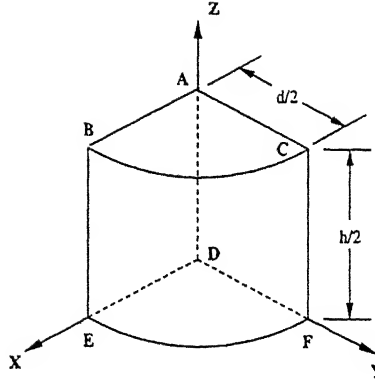


Figure 3.1: Domain used for axisymmetric upsetting

3.1 Predictions using Critical Damage Criterion [Dhar et al.]

3.1.1 Axisymmetric upsetting - cylindrical workpiece

In this section, effect of process variables on the reduction at which micro-crack gets initiated is presented using the critical damage criterion of Dhar et al. The properties of the material used for this study are:

Material: AISI-1090 steel

$$\bar{\sigma} = 1115\bar{\epsilon}^{0.19}$$

Initial yield stress $(\sigma_y)_0 = 464.00$ MPa,

Modulus of elasticity $E = 210$ GPa,

Poisson's ratio $\nu = 0.3$.

A uniform mesh of tetrahedron elements with 0.1 mm increment size are used. Three critical reductions are considered, when the damage variable D reaches the critical value of 0.05 at (I) free edge of the die-work interface of the workpiece (i.e., BC), (II) center of the workpiece (i.e., point D) and (III) outer corner of the mid-surface (meridian surface) of the workpiece (i.e., EF) (see fig 3.5). These reductions are 24%, 28% and 35.2% respectively.

For a typical set of process variables figures 3.5, 3.6 and 3.7 show the damage distribution at three different Reductions mentioned above. These figures show that damage becomes critical, first at the free edge of the interface of the workpiece and with further deformation at the center of the workpiece (point D). With further increase in reduction, damage at the meridian surface (i.e. EF) reaches 0.05 and damage at the same time reaches more than 0.05 throughout the workpiece except in a small region near around

point A of fig 3.5. Equivalent strain distribution at 24% reduction is shown in figure 3.8. From this it is clear that the maximum damage at the free edge of the interface is due to severe deformation. Hence high strains are here and at the center of the workpiece, are minimum. Thus, the micro-cracks will first occur at the free edge of the interface of the workpiece, then at the center of the workpiece and finally at the meridian surface. Some experimental results show that the fracture occurs at the meridian surface. To understand this hydrostatic stress and circumferential stress σ_θ distributions are discussed.

Figures 3.9, 3.10 and 3.11 show the distributions of hydrostatic stress at different reductions where micro-crack initiates at sites I, II and III respectively. From these figures, it is clear that the hydrostatic stress is minimum at the meridian surface of the workpiece, quite high at center of the workpiece and maximum at the free edge of the interface of the workpiece. Thus, the possibility of fracture is high at meridian surface. As the reduction is increased, the hydrostatic stress reduces at the meridian surface and increases at the other two locations.

Figures 3.12, 3.13 and 3.14 show the circumferential stress (σ_θ) at various reductions mentioned above. From these figures, it is clear that circumferential stress (σ_θ) is tensile at the meridian surface, while it is compressive at the free edge of the die-work interface of the workpiece and at the center of the workpiece. As the reduction increases circumferential stress (σ_θ) becomes more tensile at the meridian surface, and becomes more compressive at the free edge of the interface and center of the workpiece. Thus, the micro-cracks initiated at the meridian surface will grow fast to fracture.

Parametric Studies

In this section, effect of the coefficient of friction and geometric ratios (height to diameter ratio) of blank, on crack occurrence are studied. The uniform mesh with tetrahedron elements with increment size of 0.1 mm are used, which are the same as used in the previous section.

Effect of Coefficient of Friction

The analysis is carried out for the three critical reductions with coefficient of friction $\mu = 0.05$ and $h/d = 1$, $h = 25mm$, then the results are compared with that for $\mu = 0.1$ described earlier.

These reductions in this case are found to be 28.8%, 32% and 36.8% when damage D becomes critical at the free edges of the interface of the workpiece (i.e., BC), the center

of the workpiece (i.e., point A) and meridian surface of the cylindrical workpiece (i.e., EF) respectively. It can be clearly seen that the reduction which can be obtained without micro-crack initiation increases with decrease in friction.

Figure 3.15 shows damage D distribution, when it becomes critical at the meridian surface. The trend is same as the typical case mentioned in the above section. Once D reaches critical value in the workpiece (i.e., free edges of the interface). For the reduction, hydrostatic stress and circumferential stress distributions are presented in figures 3.16 and 3.17. Again the pattern is the same as typical case presented in the above section.

Further the analysis is carried for the coefficient of friction $\mu = 0.2$ and $h/d = 1$, $h = 25\text{mm}$, then compared with that for $\mu = 0.1$. The corresponding reductions in this case are 18.4%, 23.2% and 30.4%, the damage becomes critical at the corresponding positions mentioned earlier. Figure 3.18 shows, how the damage will vary with change in friction. It can be clearly seen that the critical damage will occur at lower reduction with increase in friction.

Effect of Geometric Ratios

The effect of geometric ratio (h/d ratio) is studied by carrying out the analysis for different cases. The analysis is carried out for the coefficient of friction $\mu = 0.1$. Three critical reductions are considered when the damage D reaches the critical value at the free edge of the die-work interface (i.e., BC), center of the workpiece (i.e., point D) and meridian surface (i.e., EF) respectively. In this analysis h/d ratios of 0.5, 0.75, 1.5 and 2 are considered.

These reductions are found to be 28.8%, 33.6%, and 40% for $h/d = 0.5$; 25.6%, 33.06% and 37.33% for $h/d = 0.75$. The corresponding reductions are found to be 24.53%, 29.33% and 36.26% for $h/d = 1.5$; 24.8%, 30.4% and 36.8% for $h/d = 2$ respectively.

For $h/d = 0.5$, figure 3.19 shows the distribution of damage at 40% reduction. The maximum damage is found to be along free edge of the interface when the damage reaches the critical value at the meridian surface. The figures 3.20 and 3.21 show the distribution of hydrostatic stress and circumferential stresses respectively for $h/d = 0.5$. The pattern of these distributions and their variations with increase in reduction are same as mentioned earlier.

For $h/d = 0.5$ and $h/d = 1$ distribution of hydrostatic stress are shown in figures 3.20 and 3.11 respectively. From this analysis the hydrostatic stress is less compressive at the meridian surface for $h/d = 1$ than compared with other cases. So this causes the crack

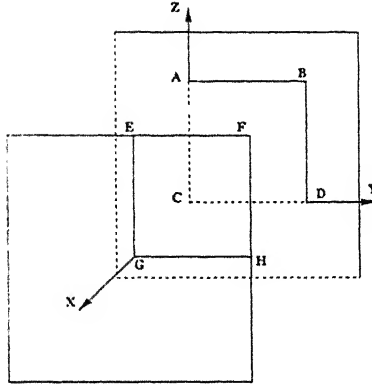


Figure 3.2: Domain used for three dimensional upsetting

initiation at lower reduction for $h/d=1$ as compared to other h/d ratio.

Figures 3.21 and 3.14 show the circumferential stress σ_θ at various geometric ratios as mentioned. From the figures it is clear that the circumferential stress is minimum compressive at the meridian surface for $h/d = 1$. Thus, it causes the initiation of micro-crack.

From the above discussions, it is clear that the micro-crack initiates at lower reduction in case of $h/d=1$, as compared to other ratios. This can be seen from figure 3.22.

3.1.2 Three dimensional upsetting - cubical workpiece

A uniform mesh of brick elements with increment size 0.1 mm are used. Three critical reductions are considered, when the damage variable D reaches the critical value of 0.05 at (I) free edges of the die-work interface of the workpiece (i.e., EF and FB), (II) center of the workpiece (i.e., point C) and (III) two corners of the meridian surface of the workpiece (i.e., point D and G). For a typical set of process variables and geometry the above mentioned reductions are found to be 24%, 28.8% and 39.2% respectively.

From the study, it is observed that the damage D becomes critical, first at the free edges of the die-work interface of the workpiece (EF and FB). With increase in reduction, D grows towards the center of the workpiece. With further increase in reduction, D at the corners of the meridian surface (i.e., point D and G) reaches 0.05 and at the same time D reaches more than 0.05 at the center of the workpiece. Figures 3.23 and 3.24 show the damage distribution at 39.2% reduction on different faces of the workpiece.

Figures 49 and 49 show the distribution of hydrostatic stress at 39.2% reduction. From these figures, it is clear that the hydrostatic stress is minimum compressive at the free edges of the die-work interface of the workpiece, and more compressive at the center of the

workpiece. Thus, the possibility of a fracture is higher at the free edges of the interface. As the reduction increases, hydrostatic stress becomes less compressive at the two corners of the meridian surface (i.e. point D and G) which enhances the growth of micro-crack initiated to fracture occurrence. At the same time, the hydrostatic stress becomes more compressive at the center of the block. Hence micro-crack initiated at this point may not grow to a fracture.

Parametric Studies

In this section, effects of the coefficient of friction and geometric ratios (height to width ratio, width to thickness ratio) of blank on crack occurrence are studied. A uniform mesh of brick elements with increment size 0.1 mm are used.

Effect of Coefficient of Friction

The analysis is carried out for the coefficient of friction $\mu = 0.2$ and $a/b = 1$, $a/h = 1$, $a = 12.5\text{mm}$. then the results are compared with that for $\mu = 0.1$ described earlier.

The critical reductions in this case are found to be 17.6%, 23.2% and 32.8% when damage D becomes critical at the free edges of the die-work interface of the workpiece (i.e., EF and FB), the center of the workpiece (i.e., point C) and two corners of the meridian surface of the workpiece (i.e., point D and G) respectively.

Figures 3.27 and 50 show the damage distribution. From figures 3.23 and 3.27, it is clear that with increase in friction, damage D reaches the critical value at lower reduction. Figures 3.29 and 3.30 show the distribution of hydrostatic stress for $\mu = 0.2$. The trend is same as the typical case mentioned in the above. With increase in friction, hydrostatic stress becomes more compressive at the center and die-work interface of the workpiece. But, it becomes less compressive at the meridian surface, which causes the fracture. From this discussion, it is clear that fracture will occur at lower reduction with increase in friction.

Effect of Geometric Ratios

The effect of different geometric ratios (a/b and a/h ratio) is studied by carrying out for the coefficient of friction $\mu = 0.1$. Three critical reductions are considered when the damage D reaches the critical value at the free edges of the die-work interface (i.e., EF and FB), center of the workpiece (i.e., point C) and corners of the meridian surface (i.e., point D and G) respectively.

Effect of a/h ratio In analysis a/h ratio of 0.5 and 1 are considered, while a/b is kept constant as 1.

These critical reductions are found to be 30.4%, 32% and 41.6% for $a/h = 0.5$, 24%, 28.8% and 39.2% for $a/h = 1$. It is observed that at $a/h = 1$, the micro-crack will initiate at lower reduction compared to other case.

For $a/h = 0.5$, figures 3.31 and 3.32 show the distribution of damage. The distribution of hydrostatic stress are shown in figures 3.33 and 3.34. From the figures it is clear that the trend is same as mentioned in typical case.

Figures 3.25 and 3.33 show the hydrostatic stress distribution at various a/h ratios. From this figures, it is clear that hydrostatic stress is more compressive at meridian surface and center of the workpiece with $a/h = 0.5$. Due to this the micro-cracks initiate at higher reduction as compared to other case.

Effect of a/b ratio In analysis a/b ratio of 0.5 and 1 are considered, while a/h is kept constant as 1.

These reductions are found to be 24.8%, 31.2% and 40.8% for $a/b = 0.5$; 24%, 28.8% and 39.2% for $a/b = 1$.

For $a/b = 0.5$, damage distribution is shown in figures 3.35 and 3.36. The maximum damage is found to be along free edge of the interface (i.e., EF).

For $a/b = 0.5$ distribution of hydrostatic stress is shown in figures 3.37 and 55. The hydrostatic stress is less compressive at the meridian surface which causes the damage at the meridian surface.

Figures 3.25 and 3.37 show the hydrostatic stress distribution at various a/b ratios. From this figures, it is clear that hydrostatic stress is more compressive at meridian surface and center of the workpiece with $a/b = 0.5$. Due to this the micro-cracks initiate at higher reduction as compared to other case.

From the above discussion, it is clear that crack initiation also depends upon geometric ratios.

3.2 Predictions using Oyane's Criterion

3.2.1 Upsetting of cylindrical workpiece

In this section, effect of process variables on the reduction at which micro-crack gets initiated is presented using Oyane's criterion. The properties of the material used for this

study are:

Material: UNI-3571 Aluminum alloy,

$$\bar{\sigma} = 574\bar{\epsilon}^{0.141}$$

Initial yield stress $(\sigma_y)_0 = 300.00$ MPa,

Modulus of elasticity $E = 70$ GPa,

Poisson's ratio $\nu = 0.33$.

A workpiece, similar to the one analyzed Dhar's criteria, is used in Oyane's criteria. Three critical reductions are considered, when the damage variable D_{oy} reaches the critical value of 0.348 at (I) free edge of the die-work interface of the workpiece (i.e., BC), (II) center of the workpiece (i.e., point D) and (III) outer corner of the mid-surface (meridian surface) of the workpiece (i.e., EF). These reductions are 19.2%, 23.2% and 33.6% respectively.

Studying this, it is clear that D_{oy} becomes critical, first at the free edge of the die-work interface of the workpiece. With increase in reduction, D_{oy} grows towards the center of the workpiece. and reaches the critical value 0.348 at the center of the workpiece. With further increase in reduction, D_{oy} at the meridian surface of the workpiece (i.e. EF) reaches 0.348 and D_{oy} at the same time reaches more than 0.348 at the center of the workpiece. The damage distribution at 33.6% reduction is shown in figure 3.39.

Figure 3.40 shows the distributions of hydrostatic stress at 33.6% reduction. Analysis of this figure shows that hydrostatic stress is less compressive as compared to other two locations. Thus, the possibility of fracture is higher at meridian surface. As the reduction is increased, the hydrostatic stress reduces at the meridian surface and increases at the other two locations.

Figure 3.41 shows the circumferential stress (σ_θ) at 33.6% reduction. Studying this figure, it is clear that (σ_θ) is tensile at the meridian surface, while it is compressive at the free edge of the interface of the workpiece and at the center of the workpiece. With increase in reduction, circumferential stress becomes more tensile at the meridian surface, and it becomes more compressive at the free edge of the interface and center of the workpiece. Thus, the micro-crack initiates at the meridian surface will grow fast to fracture.

Parametric Studies

In this section, effect of the coefficient of friction and geometric ratios (height to diameter ratio) of blank, on crack occurrence are studied. The uniform mesh with tetrahedron elements with increment size of 0.1 mm are used, which are the same as used in the

previous section.

Effect of Coefficient of Friction

The analysis is carried out for the three critical reductions with coefficient of friction $\mu = 0.05$ and $h/d = 1$. $h = 25mm$, then the results are compared with that for $\mu = 0.1$ described earlier.

These reductions in this case are found to be 24%, 26.4% and 37.6% when damage D_{oy} becomes critical at the free edges of the interface of the workpiece (i.e., BC), the center of the workpiece (i.e., point A) and meridian surface of the cylindrical workpiece (i.e., EF) respectively. It can be clearly seen that the reduction which can be obtained without micro-crack initiation increases with decrease in friction.

Figures 3.42, 3.43 and 3.44 show the growth of damage D_{oy} , hydrostatic stress and circumferential stress distribution. Again the pattern is the same as basic case mentioned in the above.

Further the analysis is carried for the coefficient of friction $\mu = 0.2$ and $h/d = 1$, $h = 25mm$, then compared with that for $\mu = 0.1$. The corresponding reductions in this case are 15.2%, 17.6% and 32.8%. Thus, with less coefficient of friction at the die-work interface, one can achieve for higher reduction without micro-crack initiation.

Effect of Geometric Ratios

In analysis, h/d ratio of 0.5, 1 and 2 are considered and the effect of geometric ratio (h/d ratio) is studied. The analysis is carried out for the coefficient of friction $\mu = 0.1$. Three typical reductions are considered when the damage D_{oy} reaches the critical value at the free edge of the die-work interface (i.e., BC), center of the workpiece (i.e., point D) and meridian surface (i.e., EF) respectively.

These reductions are found to be 24%, 27.2%, and 35.2% for $h/d = 0.5$; 19.2%, 23.2% and 33.6% for $h/d = 1$; 20.8%, 25.6% and 35.6% for $h/d = 2$.

For $h/d = 0.5$, figure 3.45 shows the distribution of damage at 35.2% reduction. The maximum damage is found to be along free edge of the die-work interface, when the damage reaches critical value at meridian surface. The figures 3.46 and 3.47 show the distribution of hydrostatic stress and circumferential stresses respectively for $h/d = 0.5$. The pattern of these distributions are same as mentioned earlier.

For $h/d = 0.5$ and $h/d = 1$ distribution of hydrostatic stress are shown in figures 3.46 and 3.40. From this analysis the hydrostatic stress is less compressive at the meridian

surface for $h/d = 1$ than compared with the other one. So this causes the crack initiation at lower reduction as compared to $h/d = 1$.

The circumferential stress σ_θ distribution is shown in figures 3.47 and 3.41 for $h/d = 0.5$ and $h/d = 1$. Studying of these figures show that the circumferential stress is less compressive at the meridian surface for $h/d = 1$. Thus, it causes the initiation of micro-cracks.

From all these analysis mentioned above, it is clear that the micro-crack initiates at lower reduction in case of $h/d=1$, as compared to other ratios.

3.3 Analysis of Backward Extrusion

In this section Cockcroft and Latham damage C_2 is discussed with the hydrostatic stress. The effect of punch nose face angle in backward extrusion is studied. Figure 3.4 shows the different types of punch profiles. The material properties, friction coefficient and blank size used in this study are as follows:

Material: UNI-3571 Aluminum alloy,

$$\bar{\sigma} = 574\bar{\epsilon}^{0.141}$$

Modulus of Elasticity $E = 70$ GPa,

Poisson's ratio $\nu = 0.33$,

Initial yield stress $(\sigma_y)_0 = 300.00$ MPa.

Two different punch models are used in this analysis, those are having the punch nose face angle of 120 and 165. The hydrostatic stress distribution for above two punch models are shown in figures 3.48 and 3.49.

The variation of hydrostatic stress at different points on the workpiece during the process is shown in figure 3.50. From this figure it is clear that the hydrostatic stress is compressive at the center of the punch-work interface during the process. The hydrostatic stress at the corner of the punch is first compressive and as the process goes on it becomes tensile. This causes the micro-crack initiation at the corner of the punch-work interface. Figure 3.51 shows the Cockcroft damage during the process at that points. It shows the damage value reaches maximum at the corner of the punch-work interface, which leads to fracture.

Figures 3.52 and 3.53 show effect of the punch nose face angle on the damage distribution at 6 mm punch travel. From these figures it is clear that the damage increases, with decrease in punch nose face angle.

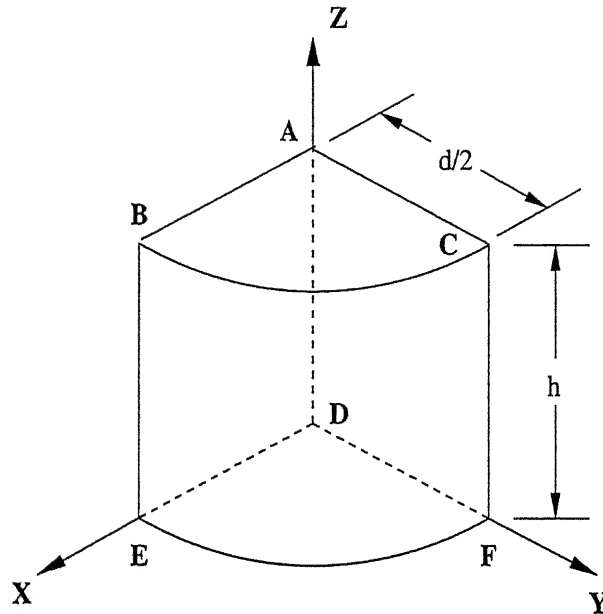
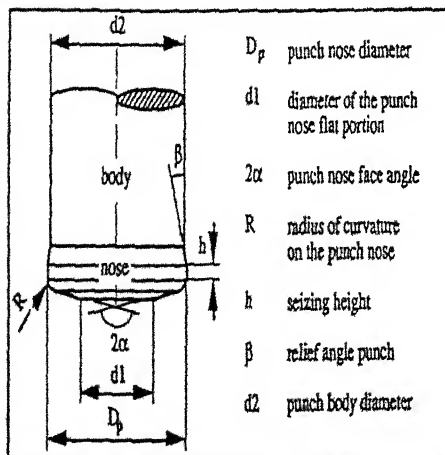


Figure 3.3: Domain used for backward extrusion



Punch dimensions	Punch1	Punch2
D_p	80 mm	80 mm
d_1	8 mm	8 mm
2α	165	120
R	6 mm	6 mm
h	4.7 mm	4.7 mm
B	5	5
d_2	79.8 mm	79.8 mm

Figure 3.4: Backward extrusion : punch dimensions

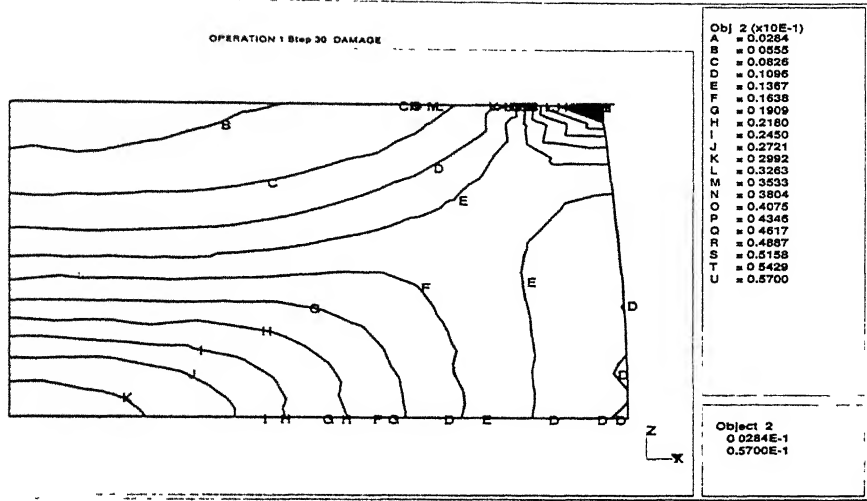


Figure 3.5: Damage distribution of cylindrical block at 24% reduction [Material AISI 1090 steel, $\bar{\sigma} = 1115\bar{\epsilon}^{0.19} + 464$ Mpa, $h = 25$ mm, $d = 25$ mm, $\mu = 0.1$]

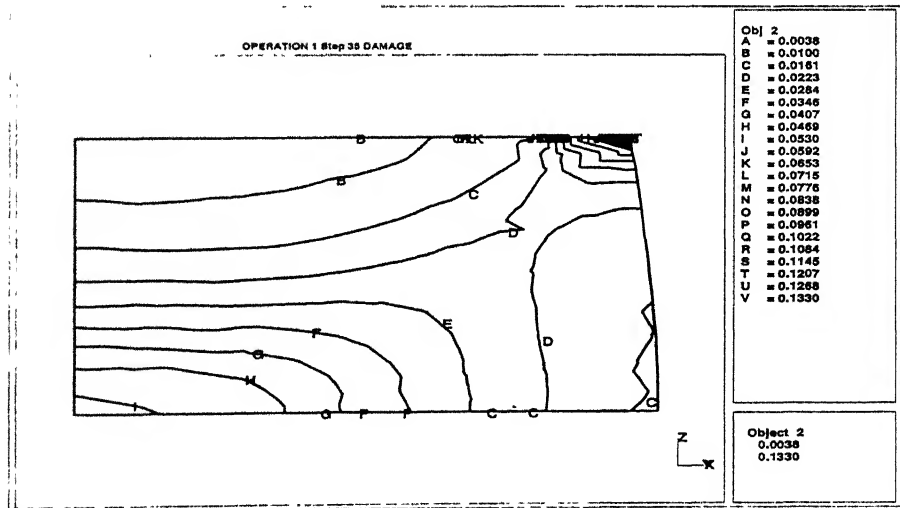


Figure 3.6: Damage distribution of cylindrical block at 28% reduction [Material AISI 1090 steel, $\bar{\sigma} = 1115\bar{\epsilon}^{0.19} + 464$ Mpa, $h = 25$ mm, $d = 25$ mm, $\mu = 0.1$]

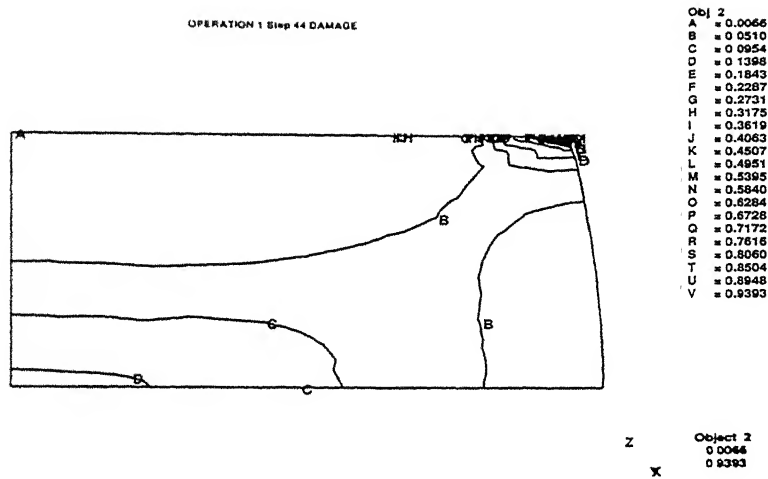


Figure 3.7: Damage distribution of cylindrical block at 35.2% reduction [Material AISI 1090 steel, $\bar{\sigma} = 1115\bar{\epsilon}^{0.19} + 464$ Mpa, $h = 25$ mm, $d = 25$ mm, $\mu = 0.1$]

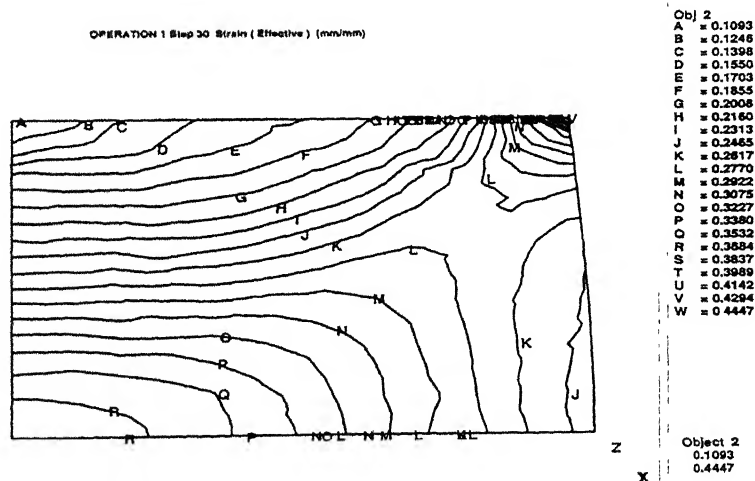


Figure 3.8: Equivalent strain distribution of cylindrical block at 24% reduction [Material AISI 1090 steel, $\bar{\sigma} = 1115\bar{\epsilon}^{0.19} + 464$ Mpa, $h = 25$ mm, $d = 25$ mm, $\mu = 0.1$]

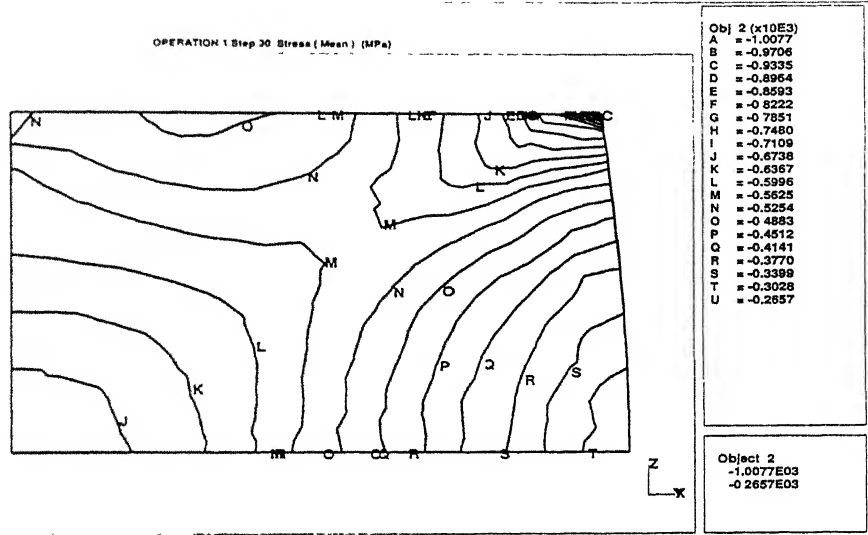


Figure 3.9: Hydrostatic stress distribution of cylindrical block at 24% reduction [Material AISI 1090 steel, $\bar{\sigma} = 1115\bar{\epsilon}^{0.19} + 464$ Mpa, $h = 25$ mm, $d = 25$ mm, $\mu = 0.1$]

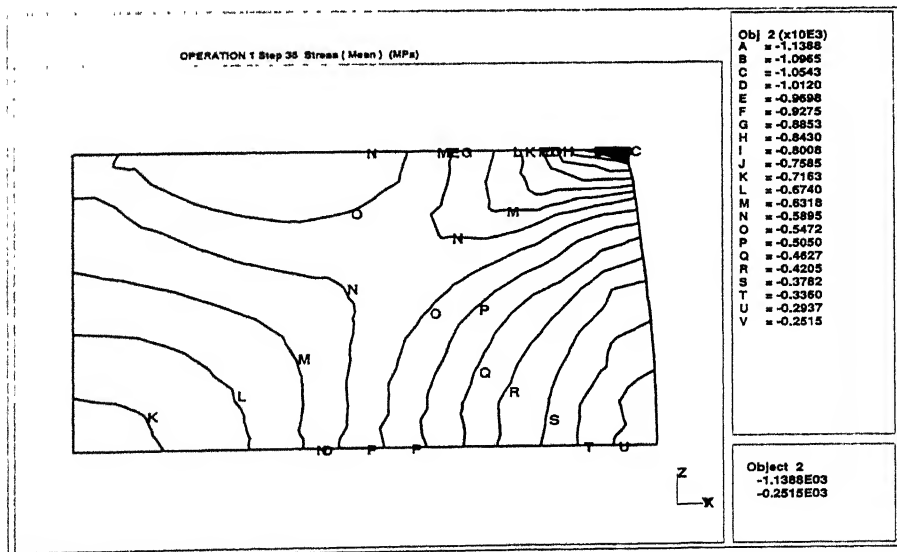


Figure 3.10: Hydrostatic stress distribution of cylindrical block at 28% reduction [Material AISI 1090 steel, $\bar{\sigma} = 1115\bar{\epsilon}^{0.19} + 464$ Mpa, $h = 25$ mm, $d = 25$ mm, $\mu = 0.1$]

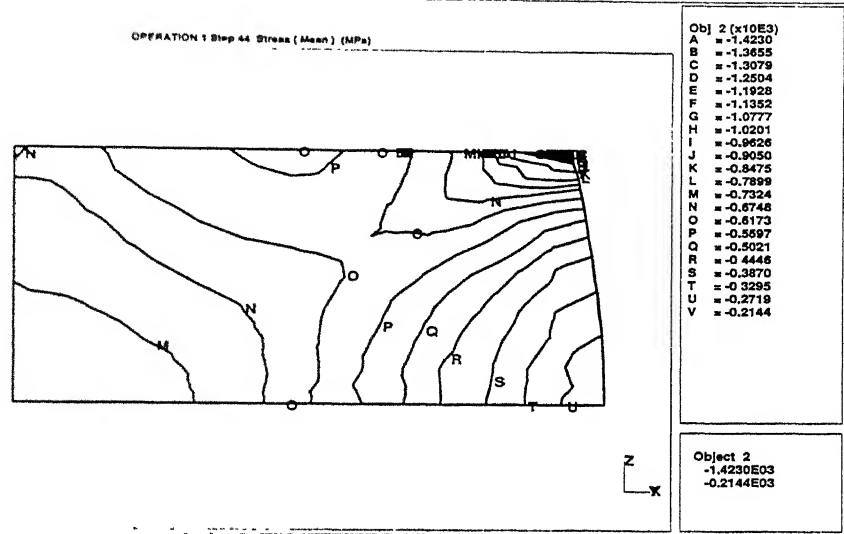


Figure 3.11: Hydrostatic stress distribution of cylindrical block at 35.2% reduction [Material AISI 1090 steel, $\bar{\sigma} = 1115\bar{\epsilon}^{0.19} + 464$ Mpa, $h = 25$ mm, $d = 25$ mm, $\mu = 0.1$]

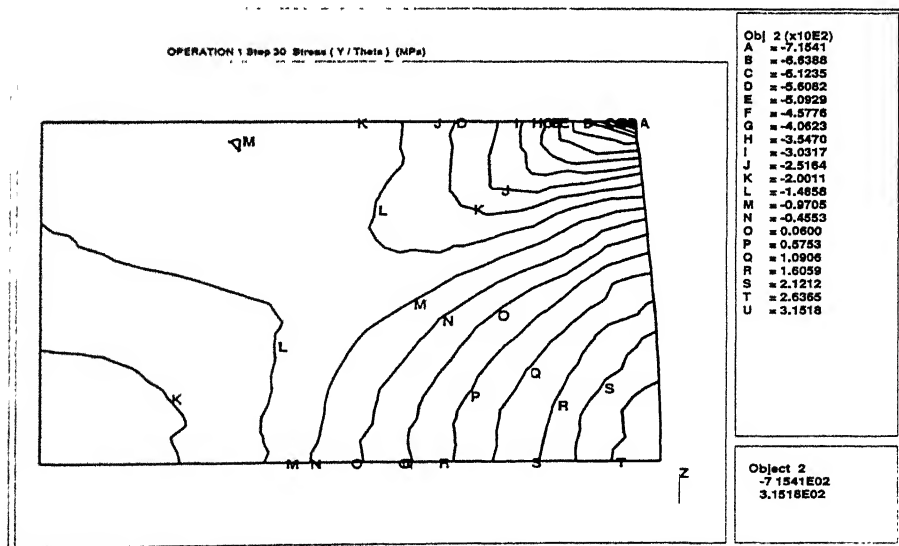


Figure 3.12: Circumferential stress distribution of cylindrical block at 24% reduction [Material AISI 1090 steel, $\bar{\sigma} = 1115\bar{\epsilon}^{0.19} + 464$ Mpa, $h = 25$ mm, $d = 25$ mm, $\mu = 0.1$]

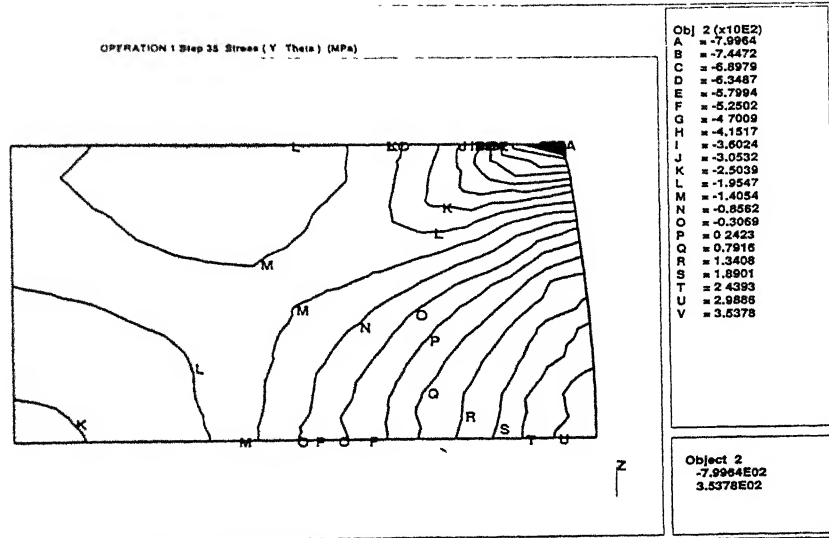


Figure 3.13: Circumferential stress distribution of cylindrical block at 28% reduction [Material AISI 1090 steel, $\bar{\sigma} = 1115\bar{\epsilon}^{0.19} + 464$ Mpa, $h = 25$ mm, $d = 25$ mm, $\mu = 0.1$]

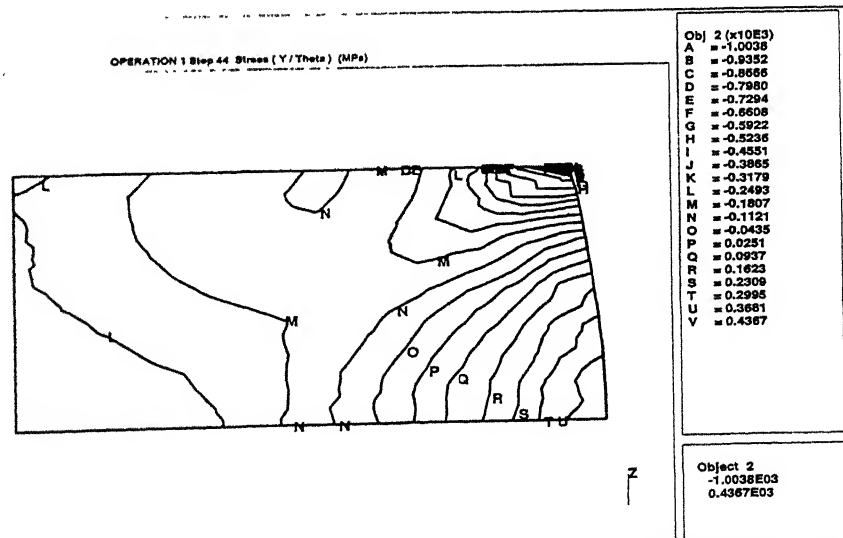


Figure 3.14: Circumferential stress distribution of cylindrical block at 35.2% reduction [Material AISI 1090 steel, $\bar{\sigma} = 1115\bar{\epsilon}^{0.19} + 464$ Mpa, $h = 25$ mm, $d = 25$ mm, $\mu = 0.1$]

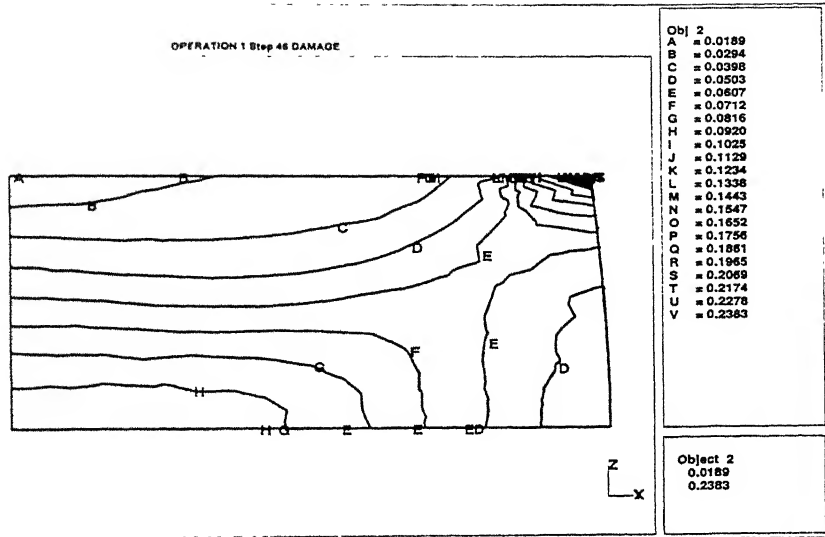


Figure 3.15: Damage distribution of cylindrical block at 36.8% reduction [Material AISI 1090 steel, $\bar{\sigma} = 1115\epsilon^{0.19} + 464$ Mpa, $h = 25$ mm, $d = 25$ mm, $\mu = 0.05$]

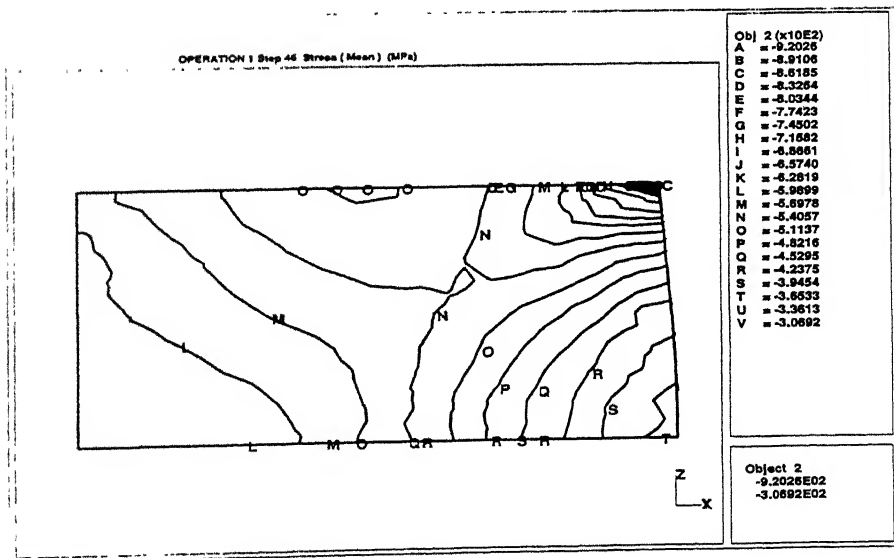


Figure 3.16: Hydrostatic stress distribution of cylindrical block at 36.8% reduction [Material AISI 1090 steel, $\bar{\sigma} = 1115\epsilon^{0.19} + 464$ Mpa, $h = 25$ mm, $d = 25$ mm, $\mu = 0.05$]

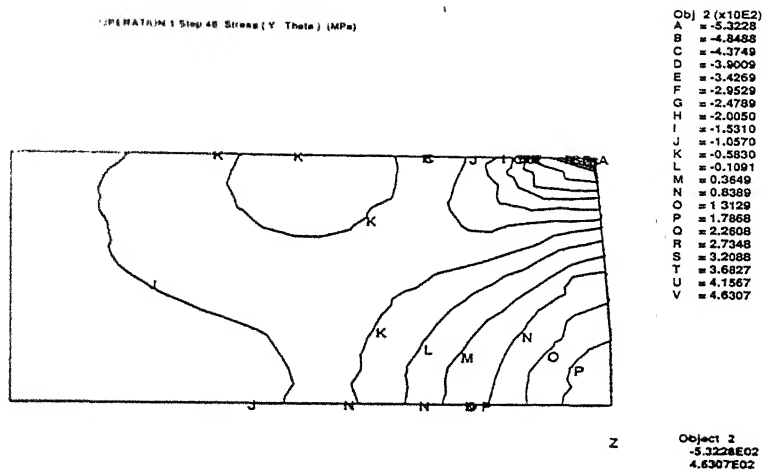


Figure 3.17: Circumferential stress distribution of cylindrical block at 36.8% reduction [Material AISI 1090 steel, $\bar{\sigma} = 1115\bar{\epsilon}^{0.19} + 464$ Mpa, $h = 25$ mm, $d = 25$ mm, $\mu = 0.05$]

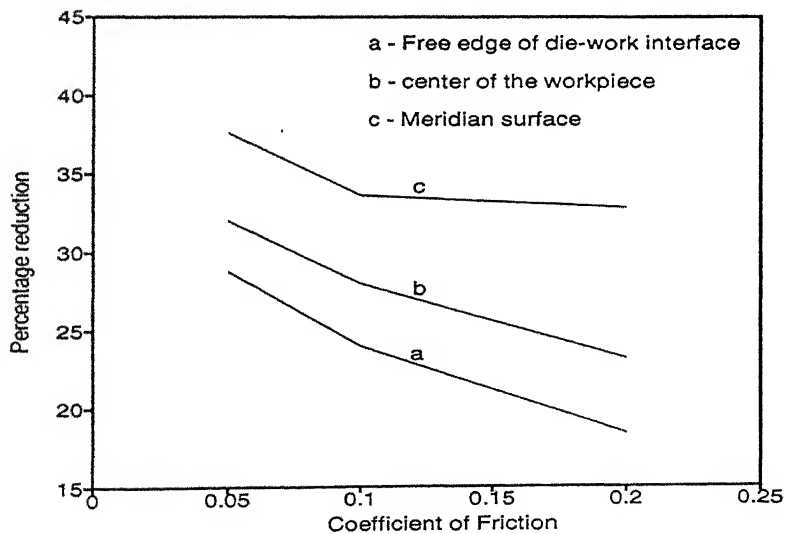


Figure 3.18: Effect of damage with varying friction [Material AISI 1090 steel, $\bar{\sigma} = 1115\bar{\epsilon}^{0.19} + 464$ Mpa, $h = 25$ mm, $d = 25$ mm]

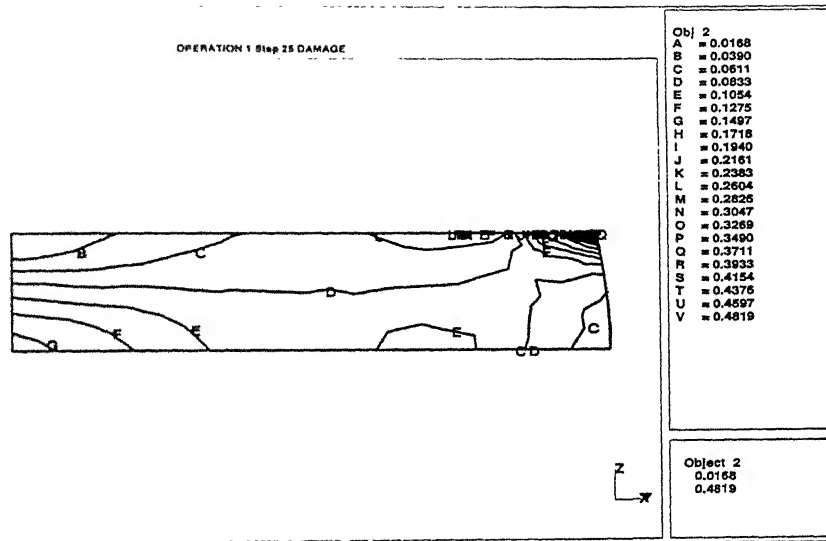


Figure 3.19: Damage distribution of cylindrical block at 40% reduction [Material AISI 1090 steel, $\bar{\sigma} = 1115\bar{\epsilon}^{0.19} + 464$ Mpa, $h/d=0.5$, $d=25$ mm, $\mu=0.1$]

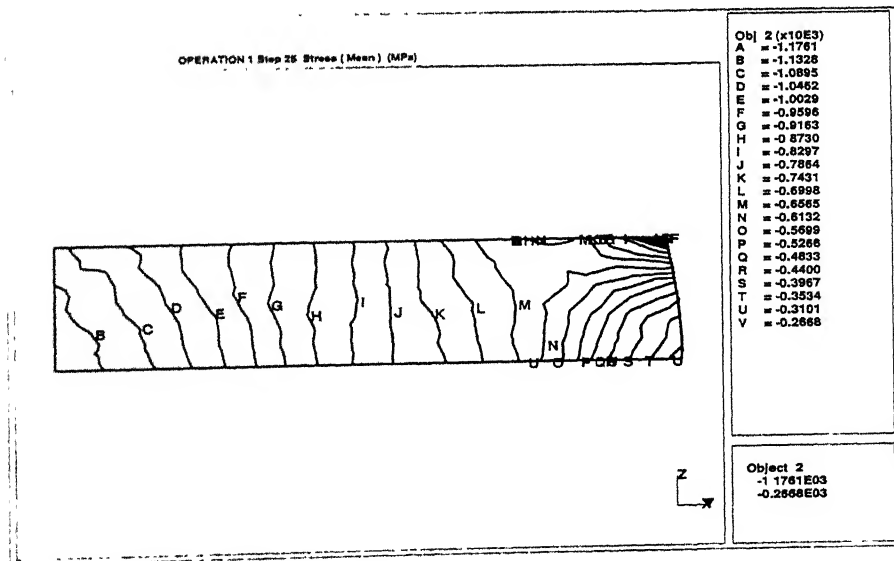


Figure 3.20: Hydrostatic stress distribution of cylindrical block at 40% reduction [Material AISI 1090 steel, $\bar{\sigma} = 1115\bar{\epsilon}^{0.19} + 464$ Mpa, $h/d=0.5$, $d=25$ mm, $\mu=0.1$]

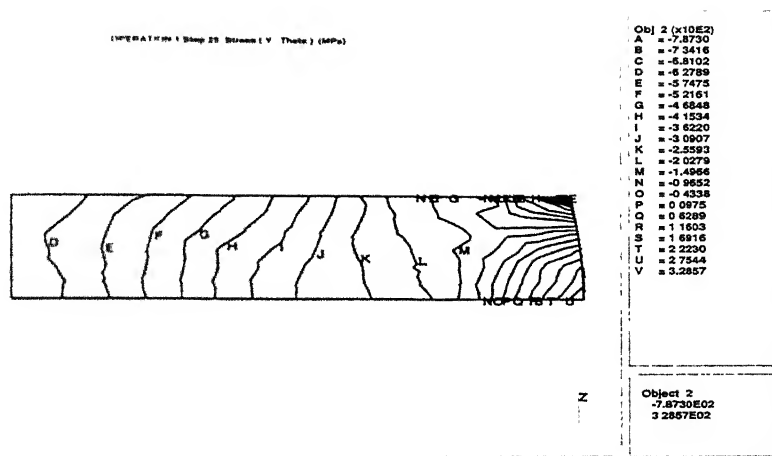


Figure 3.21: Circumferential stress distribution of cylindrical block at 40% reduction [Material AISI 1090 steel, $\bar{\sigma} = 1115\bar{\epsilon}^{0.19} + 464$ Mpa, $h/d=0.5$, $d=25$ mm, $\mu=0.1$]

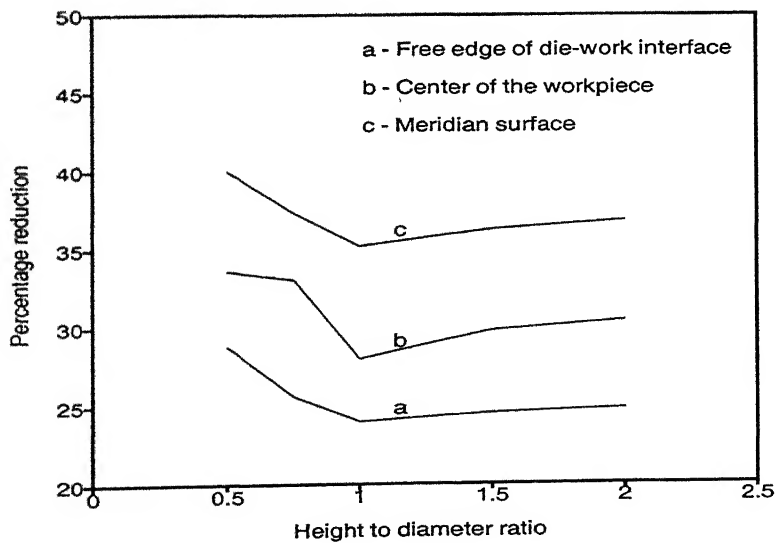


Figure 3.22: Effect of damage with varying geometric ratios [Material AISI 1090 steel, $\bar{\sigma} = 1115\bar{\epsilon}^{0.19} + 464$ Mpa, $\mu = 0.1$]

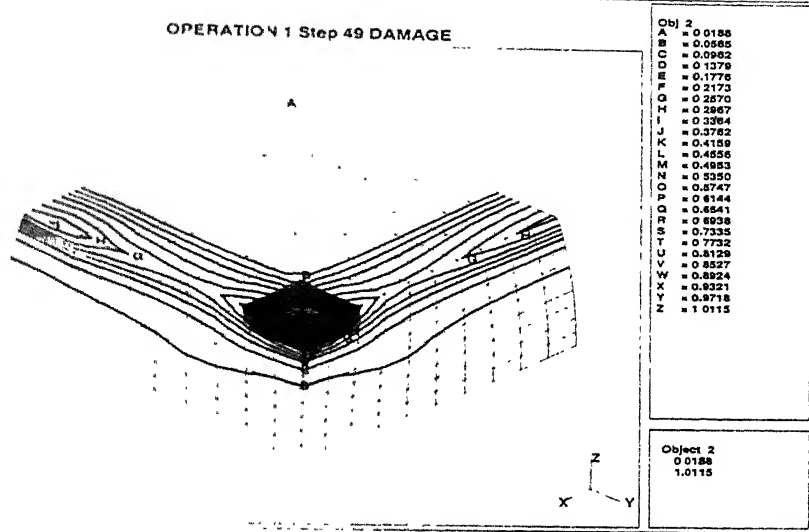


Figure 3.23: Damage distribution at the interface of cubical block at 39.2% reduction [Material AISI 1090 steel, $\bar{\sigma} = 1115\bar{\epsilon}^{0.19} + 464$ Mpa, $2h= 25\text{mm}$, $2a= 25$ mm, $2b= 25\text{mm}$, $\mu= 0.1$]

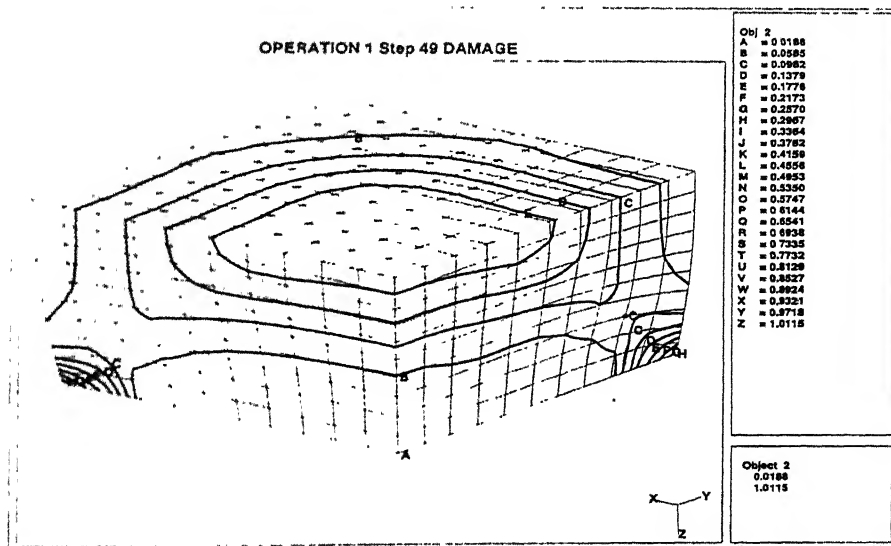


Figure 3.24: Damage distribution at the center of cubical block at 39.2% reduction [Material AISI 1090 steel, $\bar{\sigma} = 1115\bar{\epsilon}^{0.19} + 464$ Mpa, $2h= 25\text{mm}$, $2a= 25$ mm, $2b= 25$ mm, $\mu=0.1$]

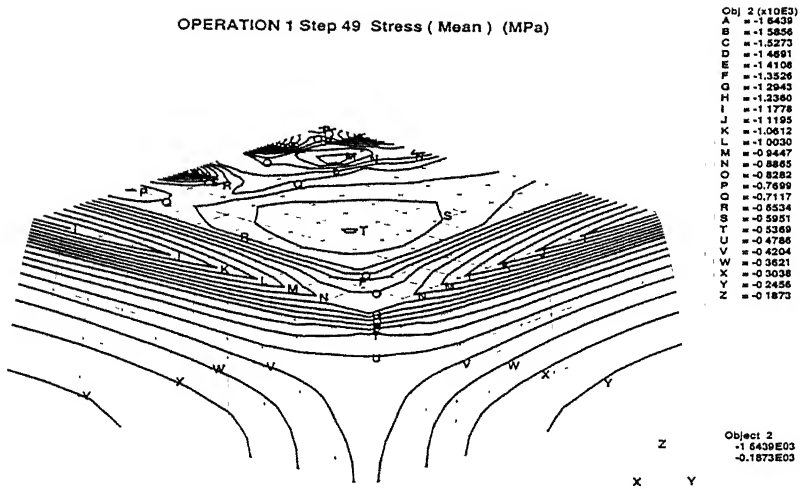


Figure 3.25: Hydrostatic stress distribution at the interface of cubical block at 39.2% reduction [Material AISI 1090 steel, $\bar{\sigma} = 1115\bar{\epsilon}^{0.19} + 464$ Mpa, $2h = 25\text{mm}$, $2a = 25\text{mm}$, $2b = 25\text{mm}$, $\mu = 0.1$]

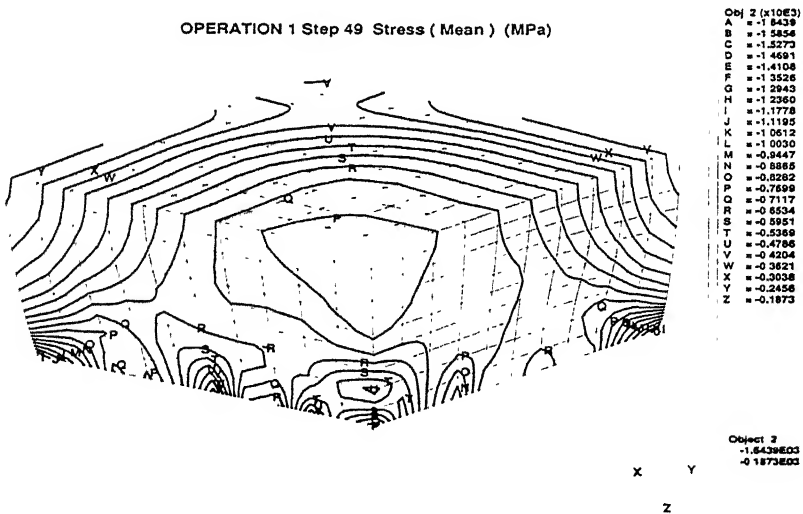


Figure 3.26: Hydrostatic stress distribution at the center of cubical block at 39.2% reduction [Material AISI 1090 steel, $\bar{\sigma} = 1115\bar{\epsilon}^{0.19} + 464$ Mpa, $2h = 25\text{mm}$, $2a = 25\text{mm}$, $2b = 25\text{mm}$, $\mu = 0.1$]

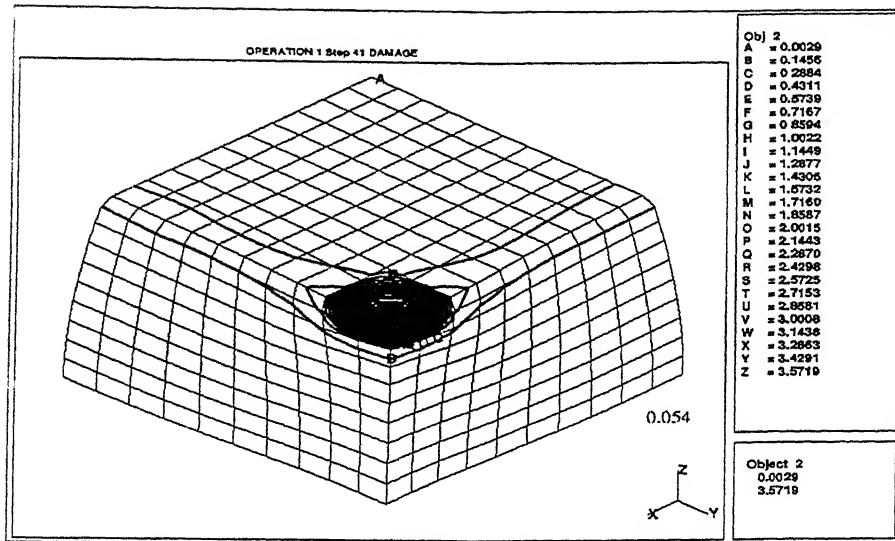


Figure 3.27: Damage distribution at the interface of cubical block at 32.8% reduction [Material AISI 1090 steel, $\bar{\sigma} = 1115\bar{\epsilon}^{0.19} + 464$ Mpa, $2h = 25$ mm, $2a = 25$ mm, $2b = 25$ mm, $\mu = 0.2$]

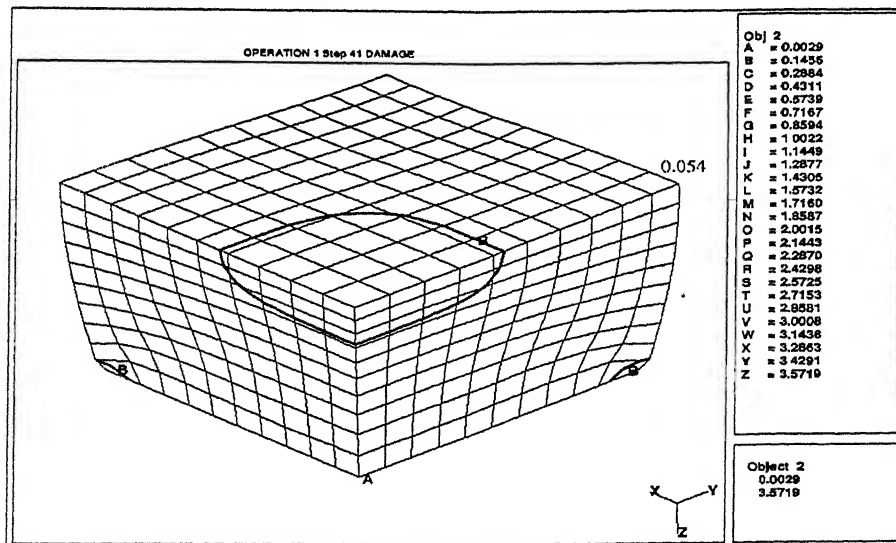


Figure 3.28: Damage distribution at the center of cubical block at 32.8% reduction [Material AISI 1090 steel, $\bar{\sigma} = 1115\bar{\epsilon}^{0.19} + 464$ Mpa, $2h = 25$ mm, $2a = 25$ mm, $2b = 25$ mm, $\mu = 0.2$]

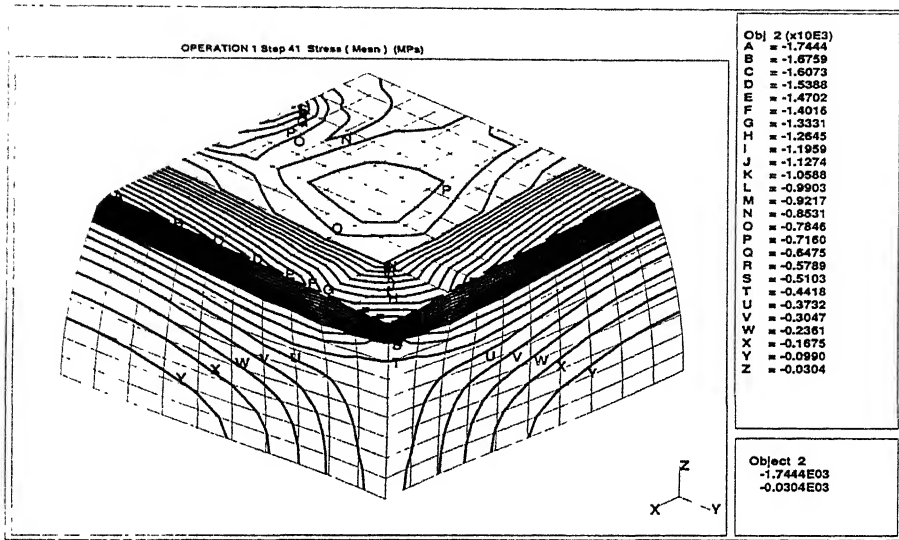


Figure 3.29: Hydrostatic stress distribution at the interface of cubical block at 32.8% reduction [Material AISI 1090 steel, $\bar{\sigma} = 1115\epsilon^{0.19} + 464$ Mpa, $2h = 25$ mm, $2a = 25$ mm, $2b = 25$ mm, $\mu = 0.2$]

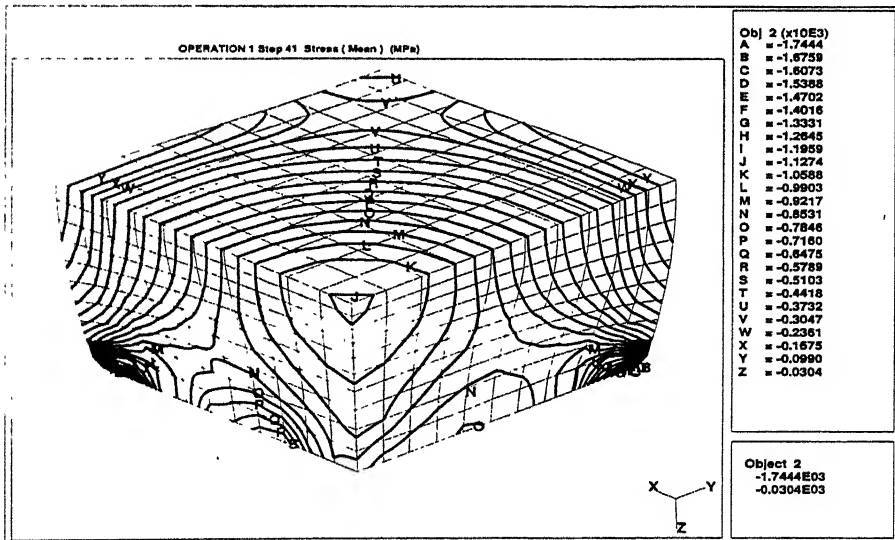


Figure 3.30: Hydrostatic stress distribution at the center of cubical block at 32.8% reduction [Material AISI 1090 steel, $\bar{\sigma} = 1115\epsilon^{0.19} + 464$ Mpa, $2h = 25$ mm, $2a = 25$ mm, $2b = 25$ mm, $\mu = 0.2$]

पुरुषोत्तम काशीनाथ केनकर पुस्तकालय

भारतीय दूरधोषकी संस्थान कानपुर

अवाप्ति क्र० A... 141871

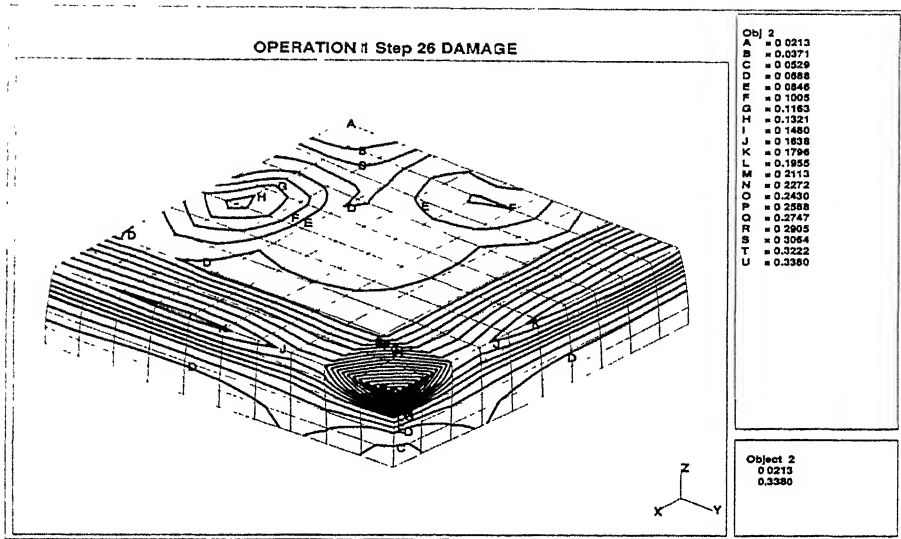


Figure 3.31: Damage distribution at the interface of cubical block at 39.2% reduction [Material AISI 1090 steel, $\bar{\sigma} = 1115\bar{\epsilon}^{0.19} + 464$ Mpa, $h/a = 0.5$, $a/b = 1$, $2a = 25$ mm, $\mu = 0.1$]

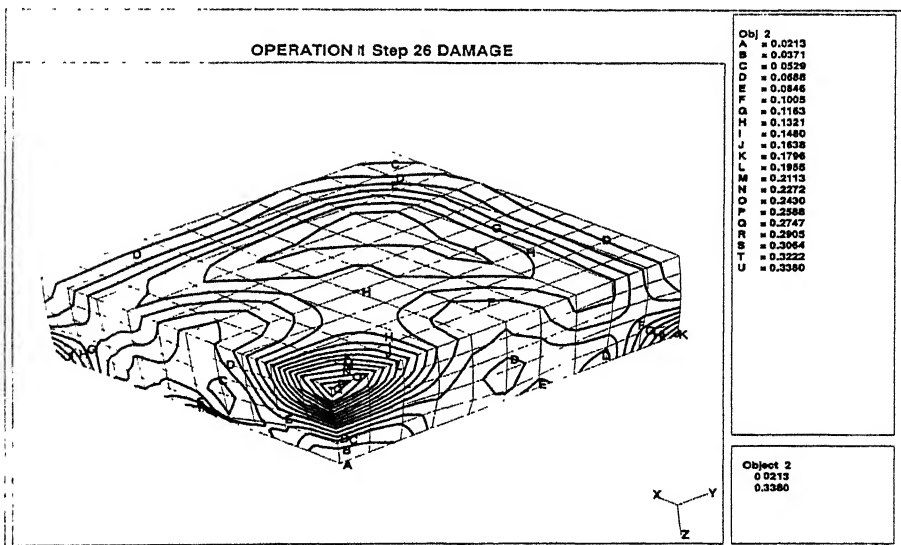


Figure 3.32: Damage distribution at the center of cubical block at 39.2% reduction [Material AISI 1090 steel, $\bar{\sigma} = 1115\bar{\epsilon}^{0.19} + 464$ Mpa, $h/a = 0.5$, $a/b = 1$, $2a = 25$ mm, $\mu = 0.1$]

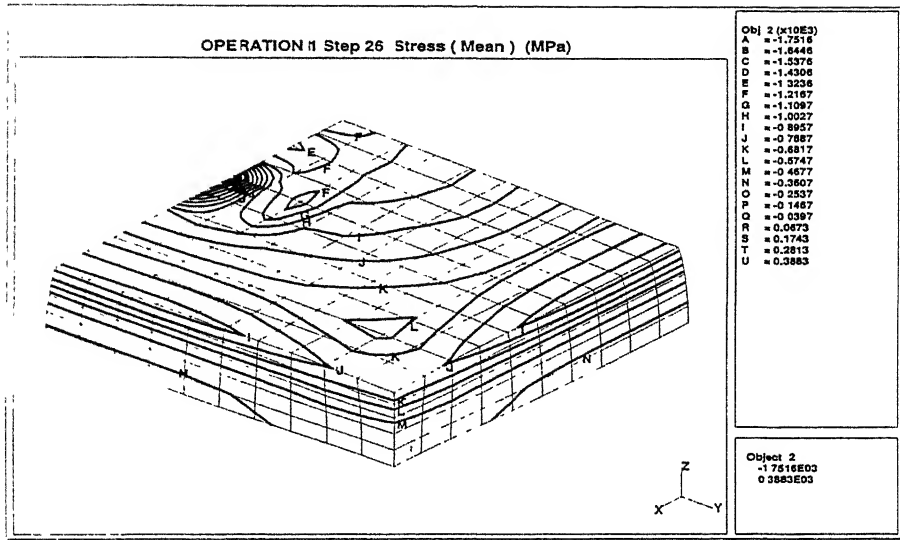


Figure 3.33: Hydrostatic stress distribution at the interface of cubical block at 39.2% reduction [Material AISI 1090 steel, $\bar{\sigma} = 1115\bar{\epsilon}^{0.19} + 464$ Mpa, $h/a = 0.5$, $a/b = 1$, $2a = 25$ mm, $\mu = 0.1$]

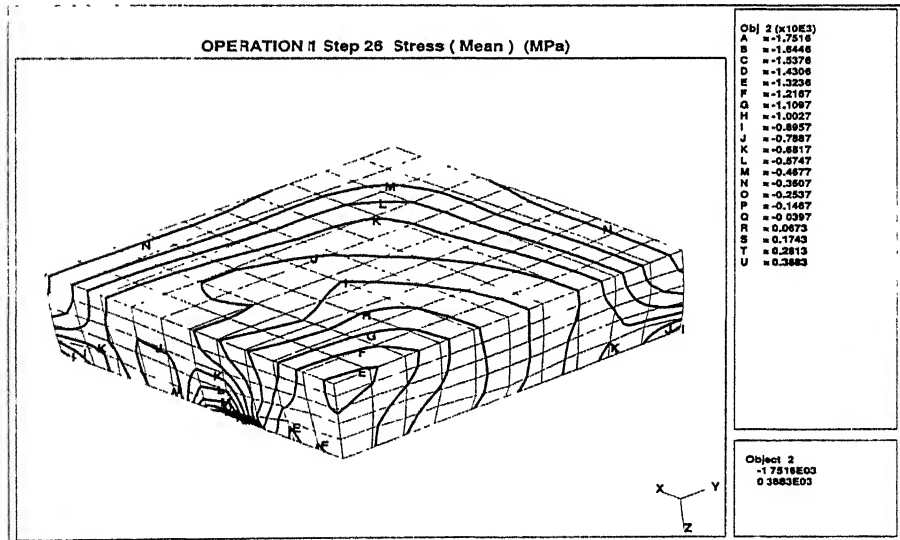


Figure 3.34: Hydrostatic stress distribution at the center of cubical block at 39.2% reduction [Material AISI 1090 steel, $\bar{\sigma} = 1115\bar{\epsilon}^{0.19} + 464$ Mpa, $h/a = 0.5$, $a/b = 1$, $2a = 25$ mm, $\mu = 0.1$]

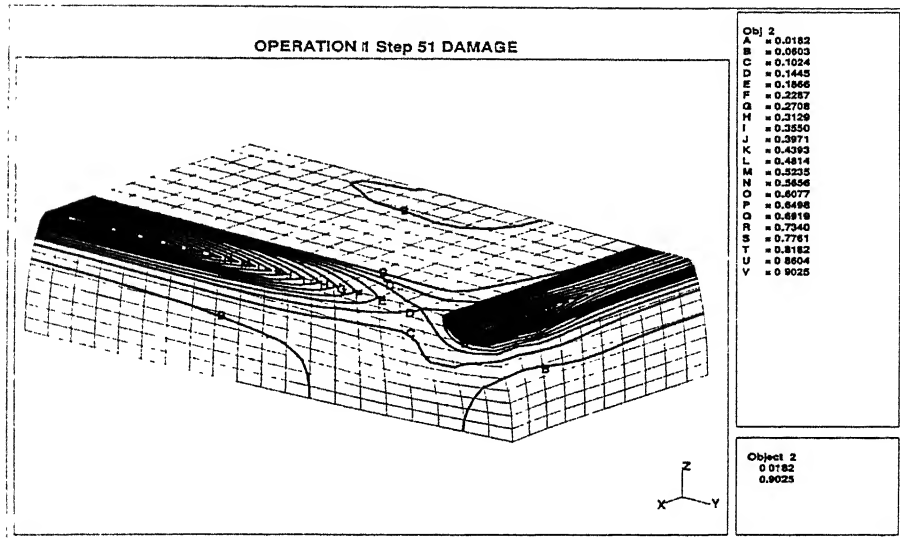


Figure 3.35: Damage distribution at the interface of cubical block at 40.8% reduction [Material AISI 1090 steel, $\bar{\sigma} = 1115\bar{\epsilon}^{0.19} + 464$ Mpa, $a/b=0.5$, $h/a=1$, $2a= 25$ mm, $\mu=0.1$]

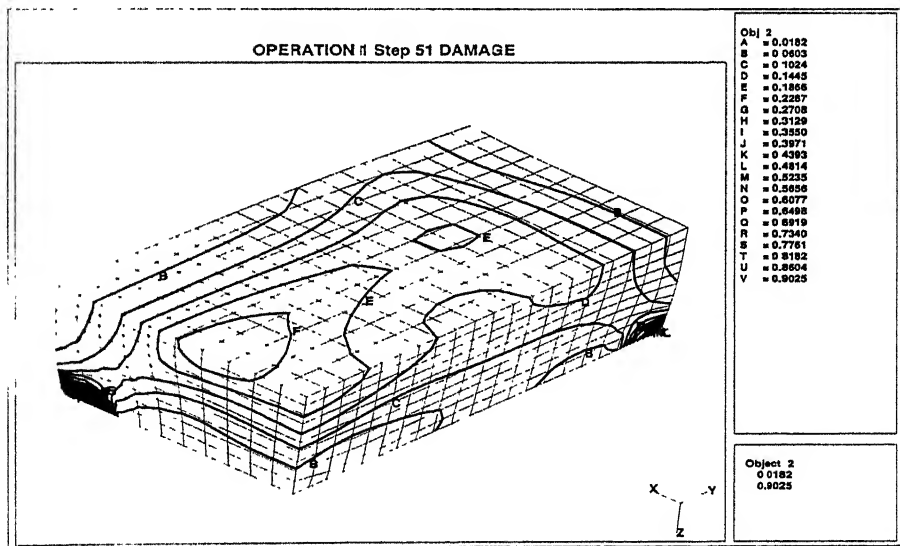


Figure 3.36: Damage distribution at the center of cubical block at 40.8% reduction [Material AISI 1090 steel, $\bar{\sigma} = 1115\bar{\epsilon}^{0.19} + 464$ Mpa, $a/b= 0.5$, $h/a= 1$, $2a= 25$ mm, $\mu=0.1$]

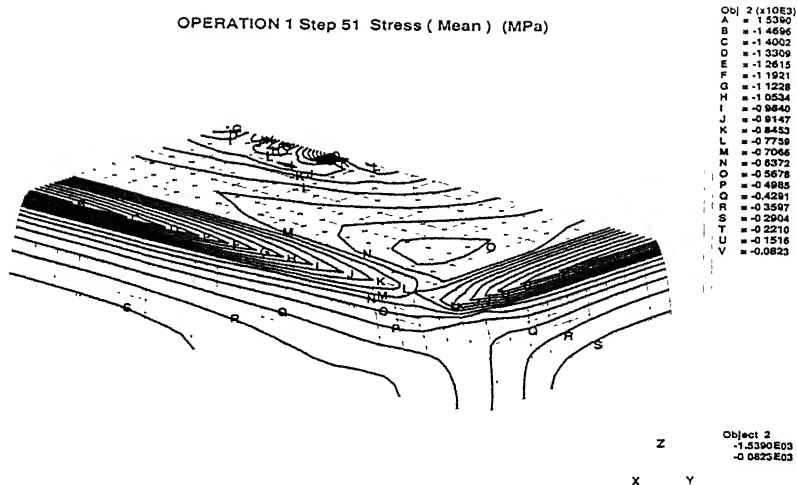


Figure 3.37: Hydrostatic stress distribution at the interface of cubical block at 40.8% reduction [Material AISI 1090 steel, $\bar{\sigma} = 1115\epsilon^{0.19} + 464$ Mpa, $a/b=0.5$, $h/a=1$, $2a=25$ mm, $\mu=0.1$]

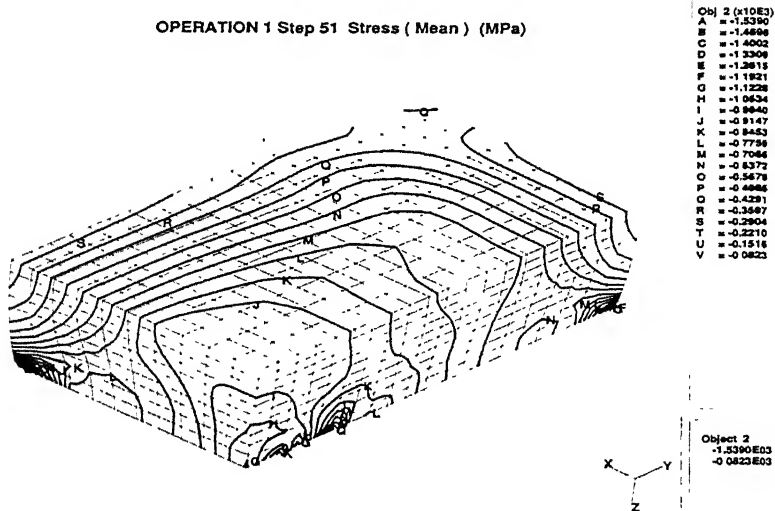


Figure 3.38: Hydrostatic stress distribution at the center of cubical block at 40.8% reduction [Material AISI 1090 steel, $\bar{\sigma} = 1115\epsilon^{0.19} + 464$ Mpa, $a/b=0.5$, $h/a=1$, $2a=25$ mm, $\mu=0.1$]

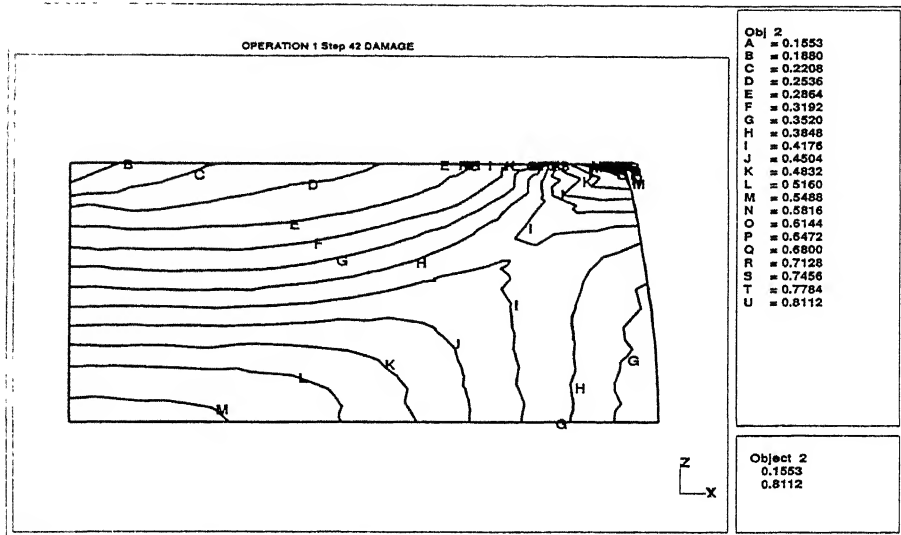


Figure 3.39: Damage distribution of cylindrical block at 33.6% reduction [Material UNI 3571, $\bar{\sigma} = 574\epsilon^{0.141} + 300$ Mpa, $h = 25$ mm, $d = 25$ mm, $\mu = 0.1$]

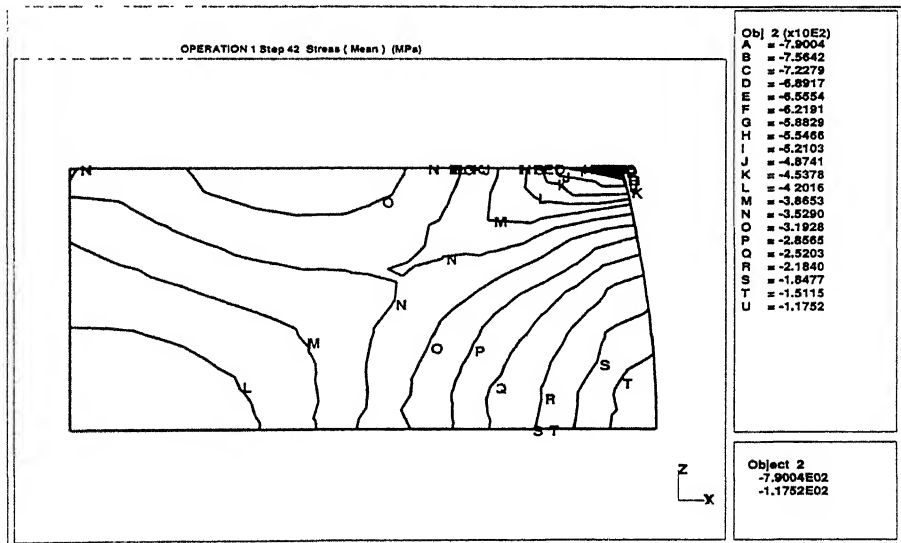


Figure 3.40: Hydrostatic stress distribution of cylindrical block at 33.6% reduction [Material UNI 3571, $\bar{\sigma} = 574\epsilon^{0.141} + 300$ Mpa, $h = 25$ mm, $d = 25$ mm, $\mu = 0.1$]

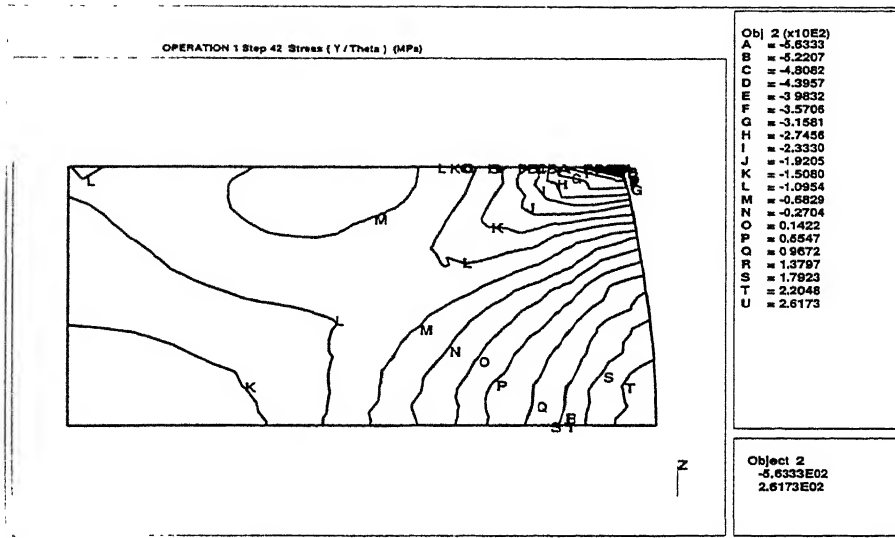


Figure 3.41: Circumferential stress distribution of cylindrical block at 33.6% reduction [Material UNI 3571, $\bar{\sigma} = 574\epsilon^{0.141} + 300$ Mpa, $h = 25$ mm, $d = 25$ mm, $\mu = 0.1$]

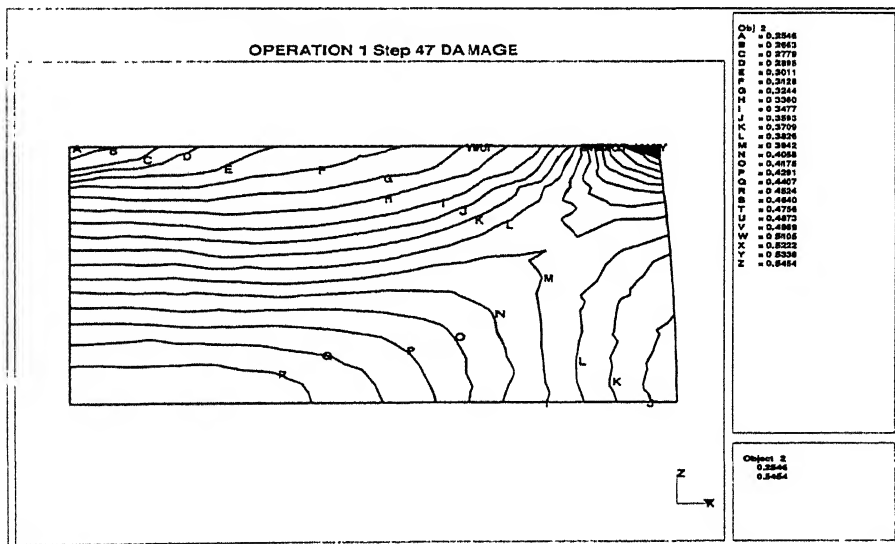


Figure 3.42: Damage distribution of cylindrical block at 37.6% reduction [Material UNI 3571, $\bar{\sigma} = 574\epsilon^{0.141} + 300$ Mpa, $h = 25$ mm, $d = 25$ mm, $\mu = 0.05$]

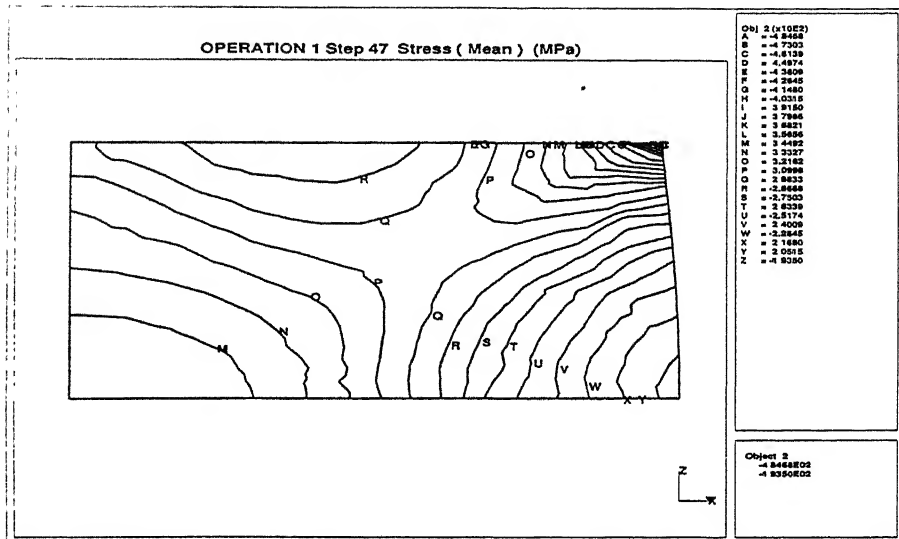


Figure 3.43: Hydrostatic stress distribution of cylindrical block at 37.6% reduction [Material UNI 3571, $\bar{\sigma} = 574\epsilon^{0.141} + 300$ Mpa, $h = 25$ mm, $d = 25$ mm, $\mu = 0.05$]

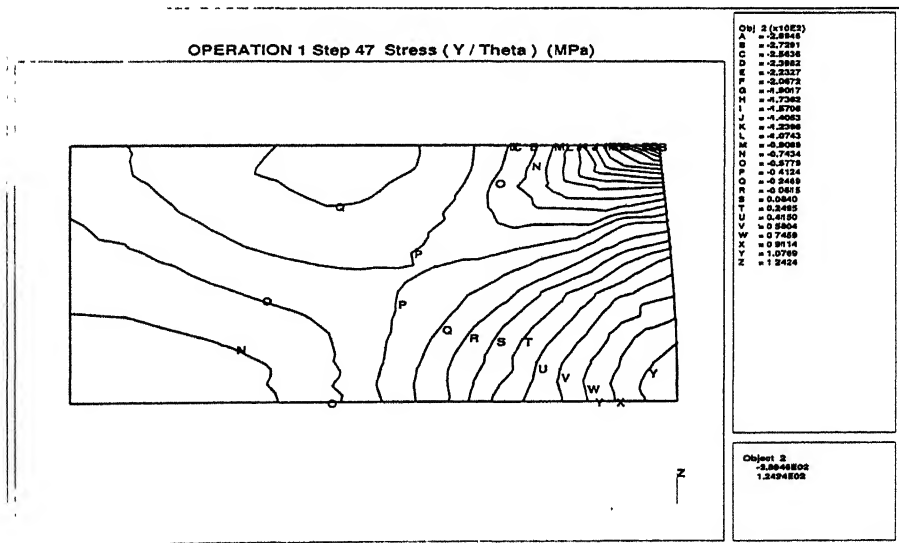


Figure 3.44: Circumferential stress distribution of cylindrical block at 37.6% reduction [Material UNI 3571, $\bar{\sigma} = 574\epsilon^{0.141} + 300$ Mpa, $h = 25$ mm, $d = 25$ mm, $\mu = 0.05$]

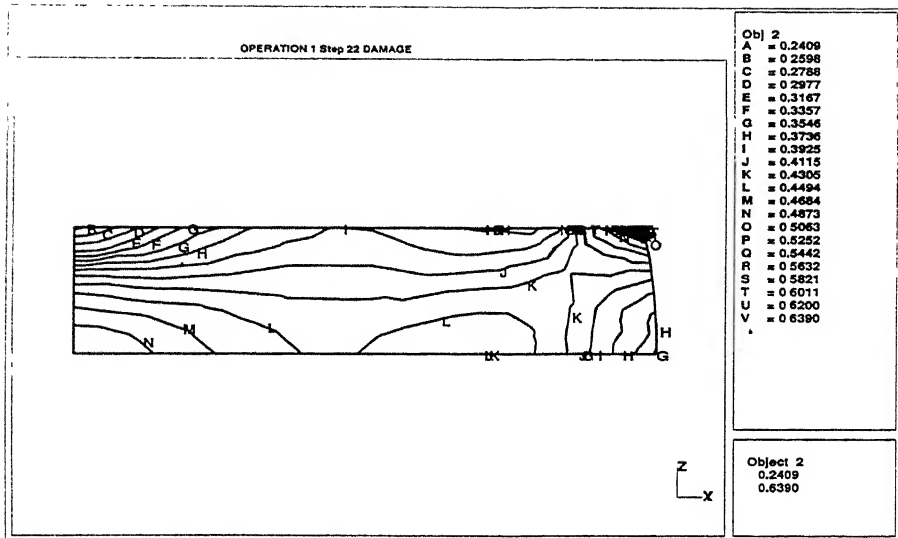


Figure 3.45: Damage distribution of cylindrical block at 35.2% reduction [Material UNI 3571, $\bar{\sigma} = 574\epsilon^{0.141} + 300$ Mpa, $h/d = 0.5$, $d = 25$ mm, $\mu = 0.1$]

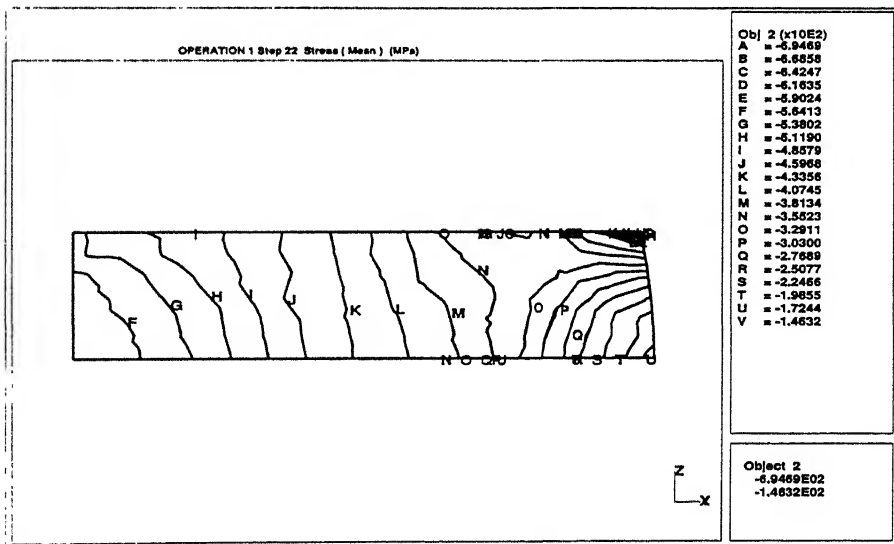


Figure 3.46: Hydrostatic stress distribution of cylindrical block at 35.2% reduction [Material UNI 3571, $\bar{\sigma} = 574\epsilon^{0.141} + 300$ Mpa, $h/d = 0.5$, $d = 25$ mm, $\mu = 0.1$]

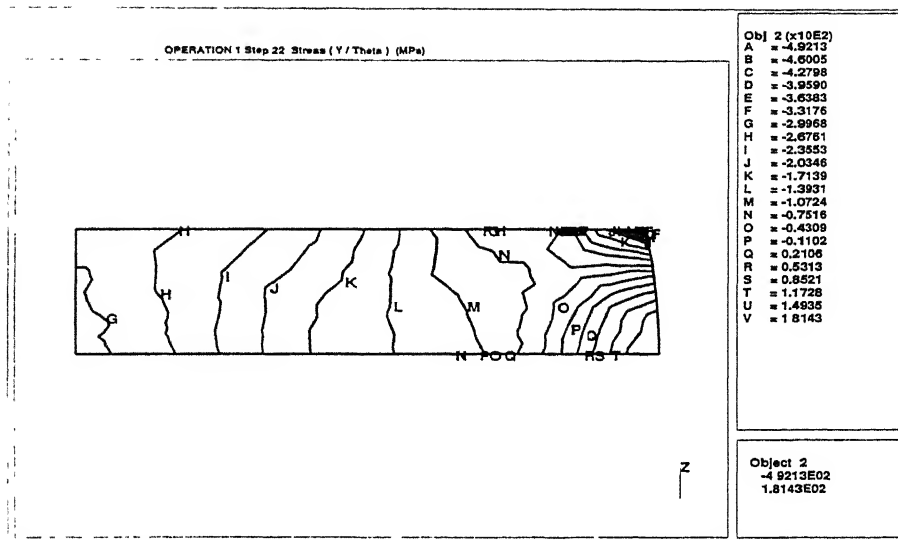


Figure 3.47: Circumferential stress distribution of cylindrical block at 35.2% reduction [Material UNI 3571, $\bar{\sigma} = 574\epsilon^{0.141} + 300$ Mpa, $h/d = 0.5$, $d = 25$ mm, $\mu = 0.1$]

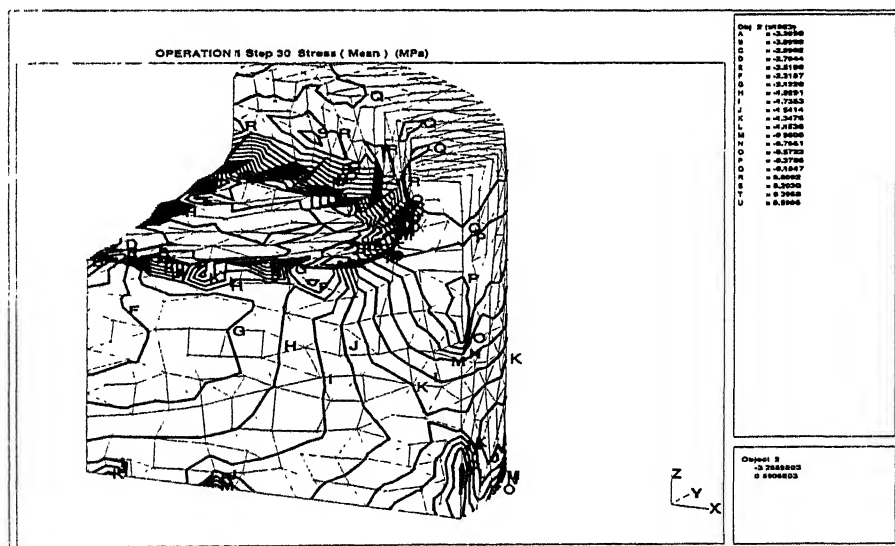


Figure 3.48: Distribution hydrostatic stress using punch 1 after 6mm movement in backward extrusion [Material UNI 3571, $\bar{\sigma} = 574\epsilon^{0.141} + 300$ Mpa, $h = 50$ mm, $d = 104$ mm, $\mu = 0.1$]

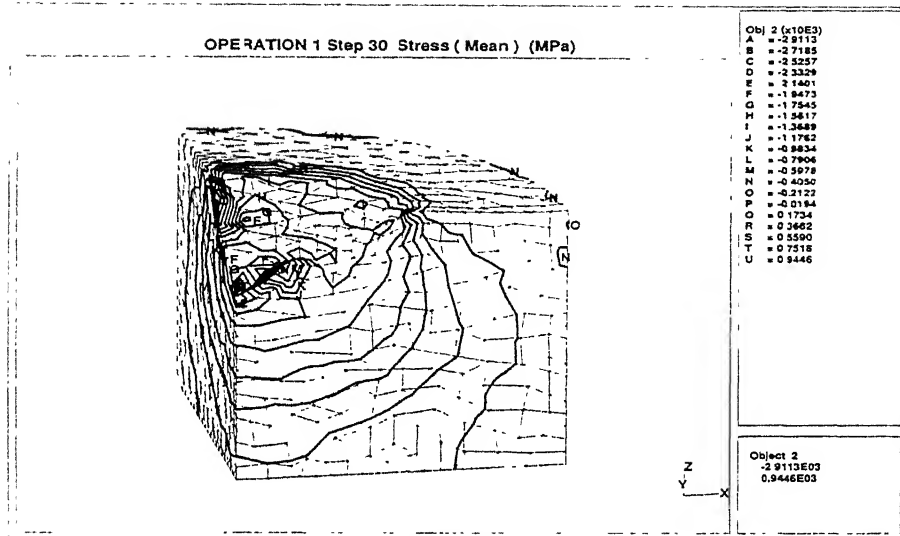


Figure 3.49: Distribution hydrostatic stress using punch 2 after 6mm movement in backward extrusion [Material UNI 3571, $\bar{\sigma} = 574\epsilon^{0.141} + 300$ Mpa, $h = 50$ mm, $d = 104$ mm, $\mu = 0.1$]

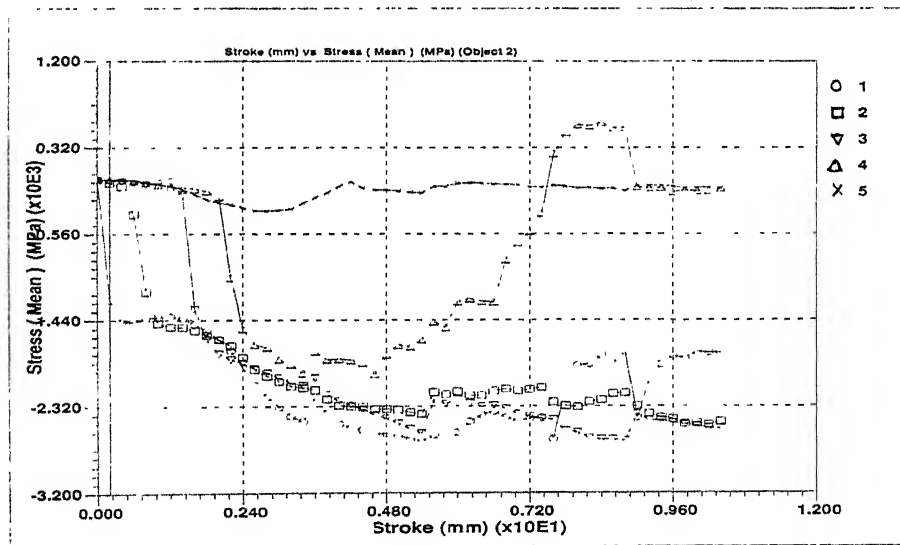


Figure 3.50: Variation of hydrostatic stress during backward extrusion process at different points [Material UNI 3571, $\bar{\sigma} = 574\epsilon^{0.141} + 300$ Mpa, $h = 50$ mm, $d = 104$ mm, $\mu = 0.05$]

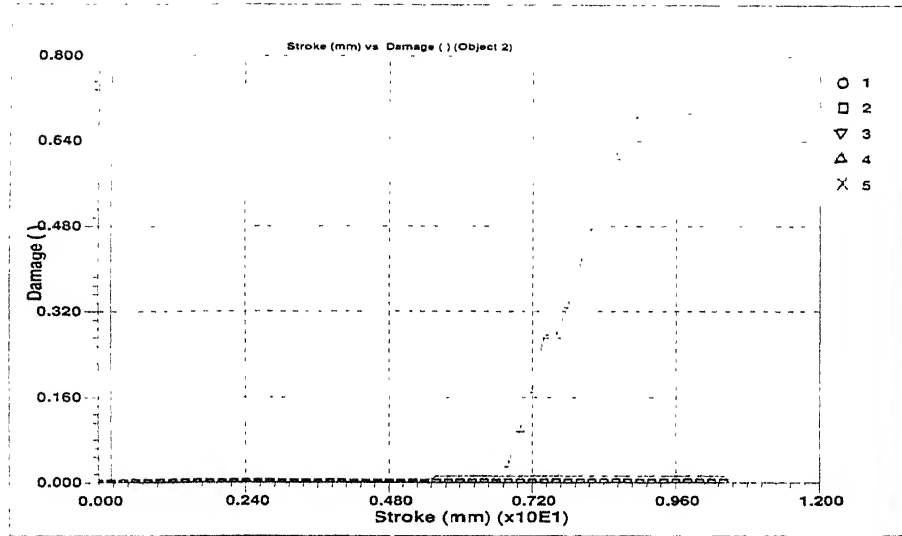


Figure 3.51: Variation of damage during backward extrusion process at different points [Material UNI 3571, $\bar{\sigma} = 574\epsilon^{0.141} + 300$ Mpa, $h = 50$ mm, $d = 104$ mm, $\mu = 0.1$]

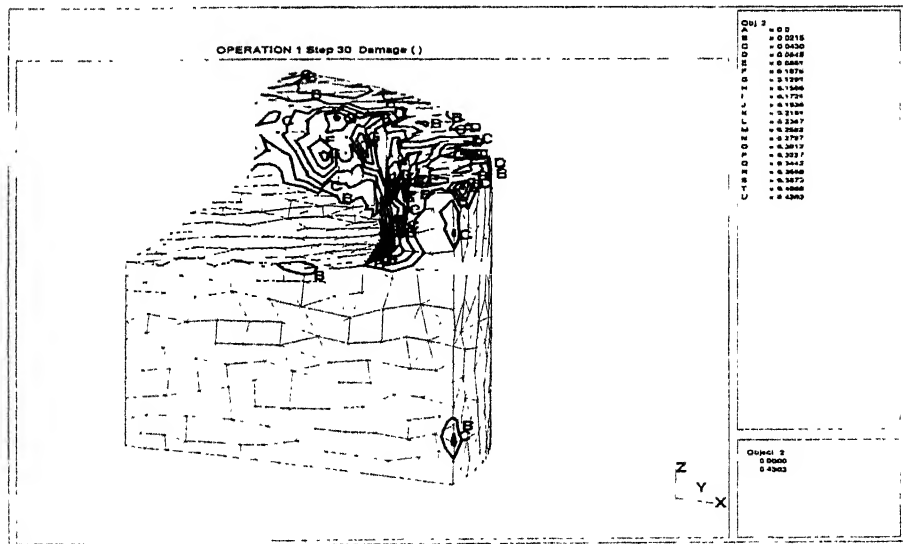


Figure 3.52: Distribution damage using punch 1, after 6mm movement in backward extrusion [Material UNI 3571, $\bar{\sigma} = 574\epsilon^{0.141} + 300$ Mpa, $h = 50$ mm, $d = 104$ mm, $\mu = 0.1$]

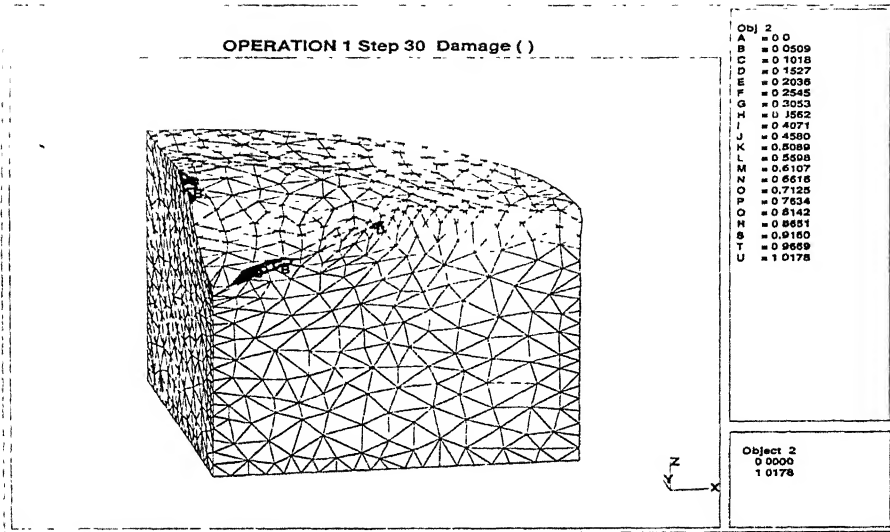


Figure 3.53: Distribution damage using punch 2, after 6mm movement in backward extrusion [Material UNI 3571, $\bar{\sigma} = 574\epsilon^{0.141} + 300$ Mpa, $h = 50$ mm, $d = 104$ mm, $\mu = 0.1$]

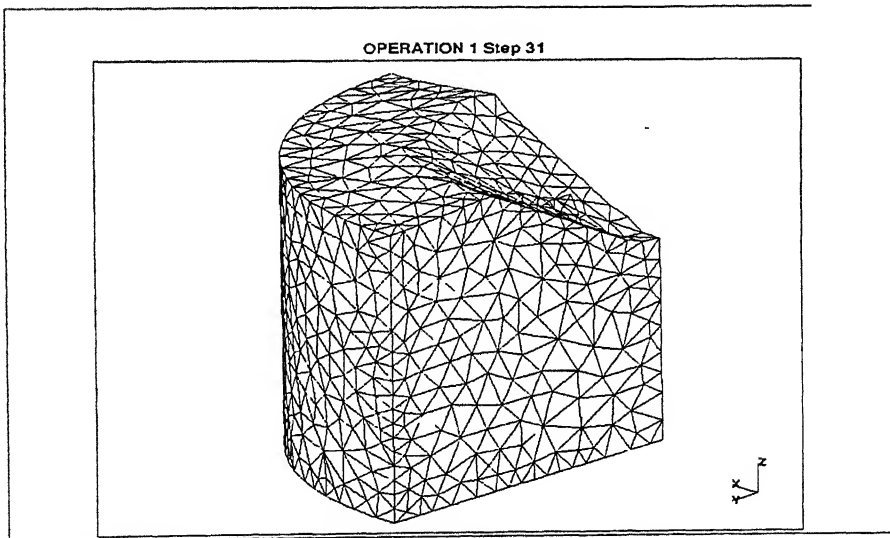


Figure 3.54: View of workpiece after 6mm movement of punch 2 in backward extrusion [Material UNI 3571, $\bar{\sigma} = 574\epsilon^{0.141} + 300$ Mpa, $h = 50$ mm, $d = 104$ mm, $\mu = 0.1$]

Chapter 4

CONCLUSIONS AND SCOPE FOR FUTURE WORK

The objective of this work is to predict the damage in various bulk metal forming processes. User defined programs are added to the DEFORM software to determine the damage. The material is assumed to be elasto-plastic strain hardening. Coulomb's friction law is used to model the friction along the die-work interface.

The occurrence of ductile fracture is the major limiting factor that determines the workability of cold bulk metal forming processes. Critical damage criterion is used to predict the damage distribution in upsetting of cylindrical and cubical workpieces. Oyane's criterion is used to predict the damage distribution in upsetting of cylindrical workpiece. For backward extrusion, Cockcroft and Latham criterion is used. A detailed parametric study of damage accumulation is carried out to show the effects of the coefficient friction and geometric ratios of the workpiece in upsetting of cylindrical and cubical workpieces. Backward extrusion is studied for various types of punch profiles.

On the basis of results presented in chapter 3, the following conclusions are made.

- The studies of damage accumulation in upsetting of cylindrical workpieces using the critical damage criterion as well as Oyane's criterion on different materials show that the micro-crack first initiates along the free edges of the die-work interface, then at the center of the workpiece and proceeded to the meridian surface. The fracture will appear first at the meridian surface since, the hydrostatic stress is minimum compressive and the circumferential stress is maximum tensile.
- From the parametric study is carried out for upsetting of cylindrical workpieces, it can be concluded that the micro-crack initiates at lower reduction as the friction

friction increases. Micro-crack initiates at lower reduction for height to diameter ratio equals to one, as compared with other values. Further, with higher height to diameter ratio, there is a possibility to form a cavity at the center of the workpiece due to minimum compressive hydrostatic stresses.

- The studies of damage accumulation in upsetting of cubical workpiece shows that, the pattern of damage and hydrostatic stress distribution is same as that of cylindrical workpiece.
- Damage evaluation in backward extrusion using Cockcroft and Latham criterion shows that the micro-crack first initiates at the corner of the punch-work interface. The hydrostatic stress at that location is first compressive and as the process goes on it becomes tensile, which aggravates the growth of micro-crack to fracture.
- From the parametric study, it is observed that with decrease in punch nose face angle, the damage value increases.

The following points may be considered as the scope for future work

- Dependence of material behavior on strain rate and temperature.
- Analysis and prediction of defects in forming processes due to residual stresses.
- Experimental studies on various metal forming processes to validate the predictions of micro-crack initiation.
- Tool deformation.

Bibliography

- [1] Aretoft, M., Wanheim, T., 1997, The basis for a design support system to prevent defects in forging, *J. Mater. Process. Tech.*, V-69, p227.
- [2] Al-Mousawi, M.M., Daragheh, A.M., and Ghosh, S.K., 1995, A Database for some Physical Defects in Metal Forming Processes, *Material Processing Defects*, (Ed. Ghosh.S.K., Predeleanu,M.), Elsevier.
- [3] Dhar, S., Raju Sethuraman, and Dixit, P.M., 1996, A Continuum Damage Mechanics Model for Void Growth and Micro Crack Initiation, *Engg. Fracture Mechanics*, V-53, 6, p917.
- [4] Dhar, S., 1995, A Continuum Damage Mechanics Model for Ductile fracture, Ph.D Thesis, Indian Institute of Technology- Kanpur(India).
- [5] Oyane, M., 1972, Criteria of Ductile Strain , *Bulletin of JSME*, 15, p1507.
- [6] Hill, R., Lee, E.H., and Tupper, S.J., 1923, A method of numerical analysis of plastic flow in plane strain and its application to the compression of a ductile material between rough plates, *Trans of ASME, J. Appl. Mech.*, V-73, p46.
- [7] Green, A.P., 1923, A Theoretical investigation of the compression of ductile material between smooth flat dies, *Philosophical Magazine Series 7* , V-42, p900.
- [8] Shabaik, A., Prediction of geometric changes of the free boundary during upsetting by slip line theory, *ASME paper no 70-WA/prd-17*.
- [9] Hoffman, O., Sachs, G., 1953, *Introduction to the Theory of Plasticity for Engineers*, Mc Graw Hill Book Company, New York.
- [10] Altan, T., 1971, Computer simulation to predict load, stress and metal flow in an axisymmetric closed die forging, in *Metal Forming*, ed. Hoffmann, A.L., Plenum press, p325.

- [11] Prager, W., and Hodge, P.G., 1951, Theory of Perfectly Plastic Solids, John Wiley, New York.
- [12] Druzer, P.C., 1954, Coulomb friction , plasticity and limit loads, Trans of ASME, J. Appl. Mech., V-21, p71.
- [13] Kudo, H., 1960, Some analytical and experimental studies of axisymmetric cold forging and extrusion-I and II, Int. J. Mech. Sci., V-2, p102.
- [14] Kudo, H., 1960, An upper bound approach to plane strain forging and extrusion -I and II, Int. J. Mech. Sci., V-2, p57.
- [15] MacDonald, A.G., Kobayashi, S., and Thomsen, E.G., 1964, Some problems of press forging lead and aluminum, Trans. of ASME, ser. B, J. Engg. for Ind., V-82, p246.
- [16] Kobayashi, S., 1964, Upper bound solution of axisymmetric forming problems, part I and II, Trans. of ASME, ser. B, J. Engg. for Ind., V-86, N, 4, p326.
- [17] Avitzur, B., 1968, Metal Forming: Processes and Analysis, McGraw Hill Book Company, New York.
- [18] Yang, D.Y., and Kim, J.H., 1987, An analysis of the three dimensional upset forging of regular polygonal blocks by using the upper bound method, Trans. of ASME, J. Engg. for Ind., V-109, p155.
- [19] Kim, J.J., Yand, D.Y., and Kim, M.U., 1987, Analysis of three dimensional upset forging of an arbitrarily shaped prismatic blocks, Int. J. Mach.Tools Manufact., V-27(3), p311.
- [20] Manuel, J.M., Barata Marques and Paulo A.F. Martins, 1991, The use of dual stream functions in the analysis of three dimensional metal forming processes, Int. J. Mech. Sci.,V-33, p313.
- [21] Lee, C.H., and Kobayashi, S., 1971, Analysis of axisymmetric upsetting and plane strain side pressing of solid cylinders by finite element method, Trans. of ASME, ser, B, J. Engg. for Ind, V-93, p445.
- [22] Shah, S.N., Lee, C.H., and Kobayashi, S., 1973, Compression of tall, circular , solid cylinders between parallel flat dies, Proc. Int. Conf. Prod. Engr., Tokyo, p295.

- [23] Chen, C.C., and Kobayashi, S., 1978, Rigid plastic finite element analysis of ring compression :applications to numerical method of forming processes, ASME, AMD, V-28, p163.
- [24] Oh, S.I., and Kobayashi, S., 1976, Workability of aluminum alloy 7075-t6 in upsetting and rolling, Trans. of ASME, ser, H, J. Engg. for Ind., V-98, p800.
- [25] Maccarini, G., Pellegrini, C., and Bugini, A., 1991, The influence of die geometry on cold extrusion forging operations: FEM and experimental results, J. Mater. process. Tech., V-27, p227.
- [26] Hartley, P., Sturgess, C.E.N., Rowe, G.W., 1979, Friction in finite element analysis of metal forming process, Int. J. Mech. Sci., V-21, p301.
- [27] Hartley, P., Sturgess, C.E.N., Rowe, G.W., 1980, Influence of friction on the prediction of forces, pressures distributions and properties in upset forging, Int. J. Mech. Sci., V-22, p743.
- [28] Shima, S., Mori, K. and Osakada, K., 1978, Analysis of Metal Forming by the Rigid Plastic Finite element Method based on Plasticity Theory for Porous Metals, Metal Forming Plasticity, ed Lippmann, H., Springer, p305
- [29] Pillinger, I., Hartley, P., Sturgess, C.E.N., and Rowe, G.W., 1985, An elastic plastic three dimensional finite element analysis of the upsetting of rectangular blocks and experimental comparison, Int. J. Mach. Tool Des. Res, V-25(3), p229.
- [30] Bathe, K.J., Ramm, E., and Wilson, E.L., 1975, Finite element formulations for large deformation dynamics analysis, Int. J. Num. Mech. Engg., V-9, p353.
- [31] Dadras, P. and Thomas, J. F. Jr, 1983, Analysis of axisymmetric upsetting based on flow pattern observation, Int. J. Mech. Sci., V-25, p421
- [32] Carter, W.T., Jr and Lee, D., 1986, Further analysis of axisymmetric upsetting, Trans. of ASME, ser, B, J. Engg. for Ind., V-108, p198.
- [33] Park, J.J., and Kobayashi, S., 1984, Three dimensional finite element analysis of block compression, Int. J. Mech. Sci., V-26(3), p165.
- [34] Surdon, G., Chenot, J. L., 1987, Finite element calculation of three dimensional hot forging, Int. J. Num. Mech. Engg, V-24, p2107.

- [35] Fu, M., and Luo, Z., 1992, The prediction of macro defects during the isothermal forging process by the rigid viscoplastic finite element method, J. Mater. Process. Tech., V-32, p599.
- [36] Terziyski, J., Aizawa, T., and Kihara, J., 1994, Three dimensional forging simulation with finite element control., J. Mater. Process. Tech., V-45, p75.
- [37] Choi, H.H., Lee, J.H., Bijun, S.K., and Kang, B.S., 1997, Development of three dimensional finite element program for metal forming and its application to precision coining. J. Mater. Process. Tech., V-72, p396.
- [38] Satyanarayan, V., 1997, Dynamic large deformation elasto plastic analysis of continua. M.Tech. Thesis, Dept. of Mech. Engg., I.I.T.Kanpur.
- [39] Avitzur, B., Hahn, W.C. Jr., and Mori, M., 1974, Analysis of Combined Backward-Forward Extrusion, Annals of CIRP, V-23, 1, p77.
- [40] Kobayashi, S., Oh, S. and Altan, T., 1989, Metal Forming and The Finite Element Method, Oxford university press, New York.
- [41] Liou, J.H., and Jang, D.Y., 1997, Forging parameter optimization considering stress distributions in products through FEM analysis and robust design methodology, Int. J. Mach. Tools. Manufact, V-37(6), p775.
- [42] Bathe, K. J., 1998, Finite Element Procedures, Prentice-Hall of India, New Delhi.
- [43] Haisler, W.E., and Stricklin, J.A., 1977, Displacement Incrementation in Non-linear Structural Analysis by the Self-Correcting Method., Int. J. Num. Meth. Engg., V-11, p3.
- [44] Batoz, J. L., and Dhatt, G., 1979, Incremental Displacement Algorithms for Non-Linear Problems, Int. J. Num. Meth. Engg., V-14(2), p1262.
- [45] Zhou, X. B., Biao, Vinh, T., and Criqui, B., 1987, Backward Extrusion - Residual Deformability of Resulphurized Mid-Hard Steels, Annals of CIRP, V-36, 1, p161.
- [46] Lin, H. H., Kawakami, K., and Kudo, H., 1988, Metal Flow Control in Cold Simulations Forward/Backward Extrusion, Annals of CIRP, V-37, 1, p231.
- [47] Park, J. S. and Hwang, S. M., 1991, Automatic Remeshing in Finite Element Simulation of Metal Forming Process by Guide Grid Method, J. Mater. Process. Tech., V-27, p73.

- [48] Park, J. S. and Hwang, S. M., 1991, Automatic Remeshing in Finite Element Simulation of Metal Forming Process by Guide Grid Method, *J. Mater. Process. Tech.*, V-27, p73.
- [49] Lee, N. K., Yoon, J. H., and Yang, D. Y., 1992, Finite Element Analysis of Large Deformation by Automatic Renoding as a Weak Remeshing Technique, *Int. J. Mech. Sci.*, V-34, 4, p255.
- [50] Bae, W. B., and Yang, D. Y., 1992, An Upper-Bound Analysis of the Backward Extrusion of Internally Elliptic-Shaped Tubes from Round Billets, *J. Mater. Process. Tech.*, V-30, p13.
- [51] Prikazsky, J. M., Hrycaj, P., Picart, P., Oudin, J., Lochegnies, D., and Ravalard, Y., 1992, Finite Element Analysis of the Three-stage Cold Extrusion of Steel Cups, *J. Mater. Process. Tech.*, V-31, p27.
- [52] Shen, G., Vedhanayagam, A., Kropp, E., and Altan, T., 1992, A Method for Evaluating Friction using a Backward Extrusion-type Forging, *J. Mater. Process. Tech.*, V-33, p109.
- [53] Tjotta, S., and Heimlund, O., 1992, Finite Element Simulations in Cold Forging Process Design, *J. Mater. Process. Tech.*, V-36, p79.
- [54] Lin, Y. T., and Wang, J. P., 1993, A New Upper Bound Elemental Technique Approach to Axisymmetric Metal Forming Processes, *Int. J. Mach. Tools Manufact.*, V-33, p135.
- [55] Ghobrial, M. I., Lee, J. Y., Altan, T., and Bay, N., 1993, Factors Affecting the Double Cup Extrusion Test for Evaluation of Friction in Cold and Warm Forging, *v-42, 1*, p347.
- [56] Bennani, B., and Oudin, J., 1995, Backward Can Extrusion of Steels: Effects of Punch Design on Flow Mode and Void Volume Fraction, *Int. J. Mach. Tools Manufact.*, V-35, 6, p903.
- [57] Ho-Joon, C., and Jin-Hwa, C., and Beong-Bok, H., 2001, The Forming Characteristics of Radial-Backward Extrusion, *J. Mater. Process. Tech.*, V-113, p141.

- [58] Lee, H. I., Hwang, B. C., and Bae, W. B., 2001, A UBET Analysis of Non-Axisymmetric Forward and Backward Extrusion, *J. Mater. Process. Tech.*, V-113, p103.
- [59] Gurson, A. L., 1977, Continuum Theory of Ductile Rupture by Void Nucleation and Growth Part 1 -Yield Criteria and Flow Rules for Porous Ductile Media, *ASME J. of Engg. Mat. Tech.*, 99, p2.
- [60] Tvergaard, V., 1981, Influence of Voids on Shear Band Instabilities Under Plane Strain Conditions, *Int. J. of Fracture*, 17, p389.
- [61] Needleman, A., and Tvergaard, V., 1984, An Analysis of Ductile Rupture in Notched Bars, *J. of Mech. and Phys. of Solids*, 32, p461.
- [62] Oyane, M., Sato, T., Okimoto, K., and Shima, S., 1980, Criteria for Ductile Fracture and their Applications, *J. of Mech. Work. Tech.*, 4, p65.
- [63] Goods, S. H., and Brown, C. M., 1979, The Nucleation of Cavities by Plastic Deformation, *Acta Metallurgica*, V-27, p1.
- [64] McClintock, F. A., 1968, A Criterion for Ductile Fracture by the Growth of Holes *ASME J. of App. Mech.*, V-90, p363.
- [65] Rice, J. R., and Tracey, D. M., 1969, On the Ductile Enlargement of voids in Triaxial Stress Field, *J. of Mech. and Phys. of Solids*, V-17, p201.
- [66] Argon, A. S., and Im, J., 1975, Separation of Second Phase Particles in Spheroidised 1045 Steel, Cu 0.6, Pct Cr Alloy and Maraging Steel in Plastic Straining, *Metallurgical Trans -A*, V-6, p839.
- [67] Gurland, J., 1972, Observation on the Fracture of Cementite Particles in Spheroidised 1.05% C Steel Deformed at Room Temperature, *Acta Metallurgica*, V-20, p735.
- [68] Dung, N. L., 1992, Three Dimensional Void Growth in Plastic Materials, *Mechanics Research Communications*, V-19, p227.
- [69] Dung, N. L., 1992, Prediction of Void Growth in Tensile Test , *Mechanics Research Communications*, V-19, p341.
- [70] Lemaitre, J., 1985, A Continuous Damage Mechanics Model for Ductile Fracture, *ASME J. of Engg. Mat. and Tech.*, V-107, p83.

- [71] Le Roy, G., Embury, J. D., Edwards, G., and Ashby, M. F., 1981, A Model of Ductile Fracture Based on the Nucleation and Growth of Voids, *Acta Metallurgica*, V-29, p1509.
- [72] Bridgman, P. W., 1964, *Studies in Large Plastic Flow and Fracture*, Harvard University Press.
- [73] Freudenthal, A. M., 1950, *The Inelastic Behaviour of Solids*, John Wiley.
- [74] Cockcroft, M. G., and Latham, D. J., 1968, Ductility and the Workability of Metals, *J. of the Institute of Metals*, V-96, p33.
- [75] Osakada, K., Mori, K., 1978, Prediction of Ductile Fracture in Cold Forging, *Annals of the CIRP*, V-27, p135.
- [76] Norris, D. M., Reaugh, J. E., Moran, B., and Quinnones, D. F., 1978, A Plastic Strain Mean Stress criterion for Ductile Fracture,, *ASME J. of Engg. Mat. Tech.*, V-100, p279.
- [77] Thomason, P.F., 1969, Tensile Plastic Instability and Ductile Fracture Criteria in Uniaxial Compression Tests, *Int. J. Mech. Sci.*, V-11, p187.
- [78] Kobayashi, S., 1970, Deformation Characteristics and Ductile Fracture of 1040 Steel in Simple Upsetting of Solid Cylinders and Rings, *J. of Engg. for Ind.*, May, p391.
- [79] Kuhn, H. A., and Lee, P. W., 1971, Strain Instability and Fracture at the Surface of Upset Cylinders, *Metallurgical Transactions*, V-2, Nov., p3197.
- [80] Hoffmann, A. L., 1971, *Metal Forming Interrelation between Theory and Practice*, Plenum press.
- [81] Johnson, W. and Mamalis, A. G., 1977, A Survey of Some Physical Defects Arising in Metal Working Processes, *Proc. 17th Int. MTDR Conf.*, Macmillan, p607.
- [82] Sowerby, R. Chandrasekaran, N. Dung, N. L. and Mahrenholtz, 1985, The Prediction of Damage Accumulation during Upsetting Tests Based on McClintock's Model.. *VDI-Forschung in Ingenieurwesen*, p51.
- [83] Clift, S. E., Hartley, P., Sturgess, C. E. N., and Rowe, G. W., 1985, Fracture Initiation in Plane Strain Forging, *Proc. 25th MTDR*, Univ. Birmingham, p413.

- [84] Dung, N. L., 1986, Fracture Initiation in Upsetting Tests, Proc. of the NUMIFORM'86 Conference, Aug., p261.
- [85] Predeleanu, M., Cordebois, J. P. and Belkhiri, L., 1986, Failure Analysis of Cold Upsetting by Computer and Experimental Simulation, Proc. of the NUMIFORM'86 Conference, Aug., p277.
- [86] Mamalis, A. G. and Johnson, W., 1987, Defects in the Processing of Metals and Composites . Computational Methods for Predicting Material Processing Defects (Ed. M. Predeleanu), Elsevier, p231.
- [87] Clift, S. E., Hartley, P., Sturgess, C. E. N., and Rowe, G. W., 1990, Fracture Prediction in Plastic Deformation Processes, Int. J. Mech. Sci., V-32, p1.
- [88] Johnson, W., 1991, Manufacturing Defects Studies Nothing Some of the Early Ideas of Robert Mallett(1810-1881), Irish Engineer- Scientist, J. Mater. Process. Tech., V-26, p97.
- [89] Zhu, Y.Y., Cescotto, S., and Habraken, A. M., 1992, A Fully Coupled Elastoplastic Damage Modeling and Fracture Criteria in Metal forming Processes., J. Mater. Process. Tech., V-32, p 197.
- [90] Lin , Z. C., and Lin, S. Y., 1993, An investigation of Ductile Fracturing in Mild Steel during Upsetting, Int. J. Mach. Tools Manufact., V-33, 1, p31.
- [91] Zhu, Y.Y., Cescotto, S., and Habraken, A. M., 1995, Modeling of Fracture Initiation in Metal Forming Processes, p155.
- [92] Atkins, A. G., 1996, Fracture in Forming, J. Mater. Process. Tech., V-56, p609.
- [93] Gouveia, B.P.P.A.A., Rodrigues, J.M.C., Martins, P.A.F., 1996, Fracture Predicting in Bulk Metal Forming., Int. J. Mech. Sci., V-38, 4, p361.
- [94] Semiatin , S.L., Goetz, T.L., Shell, E.B., Seetharaman, V. and Ghosh, A.K., 1999, Cavitation and Failure during Hot Forging of Ti-6Al-4V, Metallurgical and Materials Transactions , V-30A, May, p1411.
- [95] Kim Hong-Seok, Im Yong-Teak and Geiger Manfred., 1999, Prediction of Ductile Fracture in Cold Forging of Aluminum Alloy, Transactions of the ASME, V-121, Aug, p336.

[96] Thomason, P.F., 1990. Ductile Fracture of Metals, Pergamon.

A

141871



A141871